



저작자표시-비영리-변경금지 2.0 대한민국

이용자는 아래의 조건을 따르는 경우에 한하여 자유롭게

- 이 저작물을 복제, 배포, 전송, 전시, 공연 및 방송할 수 있습니다.

다음과 같은 조건을 따라야 합니다:



저작자표시. 귀하는 원저작자를 표시하여야 합니다.



비영리. 귀하는 이 저작물을 영리 목적으로 이용할 수 없습니다.



변경금지. 귀하는 이 저작물을 개작, 변형 또는 가공할 수 없습니다.

- 귀하는, 이 저작물의 재이용이나 배포의 경우, 이 저작물에 적용된 이용허락조건을 명확하게 나타내어야 합니다.
- 저작권자로부터 별도의 허가를 받으면 이러한 조건들은 적용되지 않습니다.

저작권법에 따른 이용자의 권리는 위의 내용에 의하여 영향을 받지 않습니다.

이것은 [이용허락규약\(Legal Code\)](#)을 이해하기 쉽게 요약한 것입니다.

[Disclaimer](#)

Ph.D Thesis
박사 학위논문

Junction Engineering of Organic Photodiodes for Color Filter-Free Image Sensors

Seongwon Yoon(윤 성 원 尹 成 元)

Department of
Energy Science & Engineering

DGIST

2020

Ph.D Thesis
박사 학위논문

Junction Engineering of Organic Photodiodes for Color Filter-Free Image Sensors

Seongwon Yoon(윤 성 원 尹 成 元)

Department of
Energy Science & Engineering

DGIST

2020

Junction Engineering of Organic Photodiodes for Color Filter-Free Image Sensors

Advisor: Professor Dae Sung Chung

Co-advisor: Professor Jongmin Choi

by

Seongwon Yoon

Department of Energy Science & Engineering

DGIST

A thesis submitted to the faculty of DGIST in partial fulfillment of the requirements for the degree of Doctor of Philosophy in the Department of Energy Science & Engineering. The study was conducted in accordance with Code of Research Ethics¹

12. 31. 2019

Approved by

Professor Dae Sung Chung
(Advisor)

(signature)

Professor Jongmin Choi
(Co-Advisor)

(signature)

¹ Declaration of Ethical Conduct in Research: I, as a graduate student of DGIST, hereby declare that I have not committed any acts that may damage the credibility of my research. These include, but are not limited to: falsification, thesis written by someone else, distortion of research findings or plagiarism. I affirm that my thesis contains honest conclusions based on my own careful research under the guidance of my thesis advisor.

Junction Engineering of Organic Photodiodes for Color Filter-Free Image Sensors

Seongwon Yoon

Accepted in partial fulfillment of the requirements for the degree of Doctor of
Philosophy.

12. 31. 2019

Head of Committee Prof. Yong Min Lee (signature)

Committee Member Prof. Dae Sung Chung (signature)

Committee Member Prof. Jongmin Choi (signature)

Committee Member Prof. Ju Hyuck Lee (signature)

Committee Member Dr. Sung Jun Lim (signature)

Ph.D/ES
201734004

윤 성 원. Seongwon Yoon. Junction Engineering of Organic Photodiodes for Color Filter-Free Image Sensors. Department of Energy Science & Engineering. 2020. 106 p. Advisors Prof. Dae Sung Chung, Co-Advisors Prof. Jongmin Choi.

ABSTRACT

The industrially first CMOS image sensor consisting of organic photodiodes (OPDs) was reported by Panasonic on Feb. 14, 2018 (<http://www.panasonic.com/global>). As such, OPDs are now moving to the commercializing stage. However, here we want to address that even this advanced organic CMOS image sensor technology still relies on panchromatic OPDs with no color readability. They only utilize organic semiconductor's high extinction coefficient and thus high degree-of-integration of thin film OPDs, which means they still use color filters with large volume and expensive processing cost. In other words, the development of a photodiode capable of maintaining the thin film form (total thickness <1 μm) while excluding the R/G/B color filters has emerged as a key issue for improving the integration of the image sensor.

In this thesis, I will suggest three approaches to realize color-selective high performance OPDs without using color filters and their image sensor arrays by employing various methods. In the first part, various polyelectrolytes were used for realizing high-performance color filter-free OPDs. By introducing polyelectrolytes as interlayers, not only surface traps of sol-gel-derived ZnO were passivated, but also work function (WF) was shifted toward the preferred direction, so that dark current could be suppressed and external quantum efficiency (EQE) could be enhanced, simultaneously.

In the second part, I will suggest Schottky junction approach with color-selective donor materials to realize color filter-free color-selective OPDs. To enhance the OPD performance, such as dark current, noise current, photocurrent, EQE, specific detectivity, linear dynamic range, and -3 dB frequency, various methods such as the introduction of a small amount of acceptor materials, or optical design for suppressing the absorption of the unwanted wavelength range. By adding a proper amount of fullerene acceptor on the donor photoactive layer, the EQE was significantly increased due to the newly created donor-acceptor interfaces. Furthermore, this boost in EQE occurred without sacrificing dark current, and therefore, specific detectivity could be significantly enhanced by nearly an order of magnitude. In case of optical design, by optimizing each constituting layer in organic Schottky photodiode structure (donor and ZnO layers), the absorption of unwanted wavelength range could be effectively minimized.

In the last part, I will suggest a new strategy to realize color filter-free, full-color organic image sensor pixel with a new diode architecture that combines a dual functional thin-film etalon-electrode and a thin-film panchromatic organic photodiode. Furthermore, because this new "etalon-electrode" strategy enables facile patterning of RGB pixel arrays simply by adjusting the thickness of constituent layers within etalon structure, we could demonstrate a full-color image capturing ability of organic image sensor without using color filters.

Keywords: Organic Photodiode, Organic Image Sensor, Junction Engineering, Etalon-electrode, High Performance

List of Contents

Abstract	i
List of Contents	ii
List of Tables	iii
List of Figures	iv
1 Introduction	1
2 Approaches for Junction Engineering	2
2.1 Work function tuning approach using polyelectrolytes	2
2.1.1 Introduction	2
2.1.2 Experimental details	4
2.1.3 Results and discussion	5
2.1.3.1 Anionic polyelectrolyte as a cathode interlayer	5
2.1.3.2 Conjugated polyelectrolytes as cathode interlayers	14
2.2 Schottky junction approach using color-selective donors	24
2.2.1 Introduction	24
2.2.2 Experimental details	28
2.2.3 Results and discussion	32
2.2.3.1 Introduction of acceptors for enhanced external quantum efficiency	32
2.2.3.2 Optical design for suppression of band II absorption	38
2.3 Etalon-electrode approach with a single photoactive layer	50
2.3.1 Introduction	50
2.3.2 Experimental details	53
2.3.3 Results and discussion	55
3 Conclusion	75
4 References	77
5 국문 요약	93

List of Tables

Table 2.1.1 Comparison of figures-of-merit for OPDs reported recently.

Table 2.2.1 Summary of the measured charge carrier mobility values of photoactive layers.

Table 2.3.1 Comparison of the suggested OPD with recently reported OPDs.

List of Figures

Figure 2.1.1 (a) UV-Vis. spectrum of the PTB7-Th:PC₇₁BM blend film and (b) the UPS spectra of the ITO/ZnO and ITO/ZnO/PSS samples.

Figure 2.1.2 (a) J - V characteristics in dark and illuminated circumstances, (b) (left panel) the specific detectivity plots under -5 V and (right panel) external quantum efficiency plots of the optimized devices under various biases as a function of wavelength, and (c) the junction resistance plots as a function of applied voltage.

Figure 2.1.3 The atomic force microscope (AFM) topography images of the devices (left panel) without and (right panel) with PSS interlayer ($5\text{ }\mu\text{m} \times 5\text{ }\mu\text{m}$).

Figure 2.1.4 The noise current distribution of the optimized OPD as a function of dark current.

Figure 2.1.5 (a) The ideality factor as a function of applied voltage and (b) linear dynamic range plots at -5 V.

Figure 2.1.6 Stability study of the dark current and specific detectivity with different interlayer. The dark current and detectivity data were collected at the bias of -5 V.

Figure 2.1.7 Chemical Structures and Synthetic Schemes of conjugated polyelectrolytes (CPEs).

Figure 2.1.8 (a) Absorption spectra of CPEs in aqueous solutions. (b–d) GIXD patterns of thin films of (b) 1T, (c) EG20, and (d) EG40. (e) Out-of-plane and (f) in-plane line-cut data

corresponding to (b–d). (g–i) NEXAFS data measured under various incident light angles of thin films of (g) 1T, (h) EG20, and (i) EG40. (j) π^* transition intensities versus incidence angle. Solid lines represent the fitted curves.

Figure 2.1.9 (a) Secondary cutoff region of UPS to show a work function shift as a result of the introduction of CPEs and (b) schematic energy level diagram to highlight the effect of CPEs for efficient hole blocking at the ZnO/PTB7-Th:PC₇₁BM interface of inverted OPDs operating under reverse bias mode.

Figure 2.1.10 (a) Dark current and photocurrent curves with various interlayers (1T, EG20, and EG40), and (b) calculated specific detectivity as a function of wavelength under -2 V bias.

Figure 2.1.11 (a) Measured noise current, (b) response plot as a function of switching frequency of light, and (c) linear dynamic range of the fabricated OPDs with EG40 as an interlayer.

Figure 2.2.1 Synthetic route of PNa6-Th.

Figure 2.2.2 (a) UV–vis absorption spectra in the solution phase (open circle) and film phase (open star) and (b) the absorption coefficient spectra of PNa6-Th and ZnO films.

Figure 2.2.3 (a) The cyclic voltammogram of the PNa6-Th. (b) the energy levels of the used materials, (c) the EQE spectra, and (d) dark current density–voltage (J - V) characteristics of various wt. % ratios of PC₆₁BM.

Figure 2.2.4 (a) J - V Characteristics and (b) noise current as a function of modulation frequency, and (c) specific detectivity spectrum of the optimized OPD.

Figure 2.2.5 (a) Bode plot, (b) linear dynamic range (LDR) plot at -1 V, and (c) normalized dark current as a function of operating temperature of devices.

Figure 2.2.6 (a) Absorption spectrum of PPDT2FBT film and (b) energy level diagram of a Schottky junction OPD device.

Figure 2.2.7 (a,b) Simulated results of light absorption of PPDT2FBT film by varying the active layer thickness, (c) measured dark J - V characteristics with various active layer thickness, and (d) the light absorption simulation results of ITO/ZnO/PPDT2FBT/MoO₃/Ag structure for deep blue incident photon by varying the ZnO layer thickness.

Figure 2.2.8 Magnified views of (a) red dash-dotted box, (b) blue dashed box in Figure 2.2.7(a) and (c) blue solid box in Figure 2.2.7(b).

Figure 2.2.9 (a) Absorption coefficient spectra of PPDT2FBT and ZnO films, (b) the UV-Vis absorption spectra of ZnO with varying the thickness of 40 nm and 140 nm and (c) the schematic of deep blue light (400 nm) absorption in case of thick ZnO layer.

Figure 2.2.10 (a) The specific detectivity spectrum measured at -1 V (red sphere) together with the absorption spectrum of PPDT2FBT film with thickness of 320 nm (purple line) and external quantum efficiency spectrum at 0 and -1 V (green dashed line and green solid line with open square, respectively), (b) the J - V characteristics, (c) the dynamic response at -1 V

together with the corresponding responsivity data, and (d) frequency responses of the optimized photodiode structure measured under various reverse biases.

Figure 2.2.11 Noise current of the optimized photodiode at -1 V.

Figure 2.2.12 The measured -3 dB frequency versus applied voltage plot.

Figure 2.2.13 Performance changes (a) after 100 times of cyclically scanned J - V characteristics under 650 nm light illumination, performance changes in (b) dark current density and (c) specific detectivity of the optimized OPD measured at -1 V for 57 days of air exposure in dark condition.

Figure 2.3.1 (a) Schematic illustration of etalon-electrode structures (left) and thickness profiles of the optimized R/G/B-selective etalon-electrodes (right), (b) simulated transmittance spectra with various Ag thicknesses, and (c) transmittance spectra with respect to central optical spacer thickness.

Figure 2.3.2 Simulated transmittance spectra of the Ag/LiF/Ag etalon electrodes with (red line with square) or without (blue line with circle) 10-nm-thick LiF anti-reflection layers on both external sides.

Figure 2.3.3 EQE spectra of the fabricated OPDs with green-selective etalon-electrodes with different Ag layer thickness.

Figure 2.3.4 (a) UV-vis absorption spectra of various ternary blend combinations consisting of P3HT, PTB7-Th, and PCBM, (b) simulated normalized amount of absorbed photons in

each constituting layer in OPD structure, (c) energy level diagram of used materials to fabricate OPD, (d) noise current and (e) noise current-based spectral response of the optimized panchromatic OPD at -1 V.

Figure 2.3.5 Dark current-based specific detectivity spectra with various composition ratios of photoactive layers under the reverse bias of 1 V.

Figure 2.3.6 Simulated normalized electric field intensity of each constituting layer in OPD structure.

Figure 2.3.7 (a) J - V Characteristics and (b) dV/dJ_d vs J_d^{-1} plot of the optimized panchromatic OPD for calculating ideality factor.

Figure 2.3.8 (a) Schematic illustration of etalon-electrode-based OPD (left) and cross-section scanning electron microscope (SEM) image of the optimized green-selective OPD (right), (b) J - V characteristics, (c) noise current-based spectral responses, and (d) LDRs of the optimized R/G/B-selective OPDs.

Figure 2.3.9 (a) dV/dJ_d vs J_d^{-1} plots of the optimized R/G/B-selective OPDs for calculating ideality factors, and (b) the noise current plots of the optimized R/G/B-selective OPDs.

Figure 2.3.10 (a) Current-time characteristics of blue-selective OPD exposure to pulsed laser

light for 18 hours, (b) J - V characteristics of the OPD before and after exposing to stability test.

Figure 2.3.11 (a) Digital camera image of the fabricated 10 columns of etalon-electrodes, (b)

measured EQE spectra of R/G/B-selective OPD pixels at -1 V, (c) a schematic illustration describing how to obtain star-shaped RGB image from R/G/B-selective OPD array, (d) configuration of OPD array which the R/G/B-pixels (black squares) were formed by sandwiching bottom R/G/B-selective etalonedelectrodes (pastel red, green and blue) and top reflective electrode (LiF:Al, gray), (e) normalized photocurrent distribution when white light was illuminated on the OPD array through a star-shaped shadow mask, and (f) collected result of normalized photocurrent distributions when red (650 nm, 31.7 $\mu\text{W}/\text{cm}^2$), green (550 nm, 29.5 $\mu\text{W}/\text{cm}^2$), and blue (450 nm, 43.1 $\mu\text{W}/\text{cm}^2$) lights were illuminated on the OPD array covered with a star-shaped shadow mask.

Figure 2.3.12 (a) Dark current and (b) dark current-based peak detectivity distributions of the 100 independent R/G/B-selective OPD pixels.

Figure 2.3.13 Normalized photocurrent distributions when the 10×10 OPD array was illuminated with various wavelengths of incident light.

1 Introduction

Recently, Complementary metal-oxide-semiconductor (CMOS) image sensors have gained great attention by showing potential in being used in various next-generation industrial fields, such as autonomous vehicles, medical imaging, machine vision, security, virtual reality, and augmented reality. In particular, as market interest in autonomous vehicles increases, there is an urgent demand for the development of image sensors with high resolution and high linear dynamic range (LDR) that can be applied in advanced driver assistance systems (ADAS). From this perspective, because the Si semiconductor does not have high absorption coefficients and wavelength selectivity due to its indirect band gap property [1], it can be said that conventional Si image sensors have significant disadvantages toward the formation of a long optical path and thus limited degree-of-integration due to a thick photoactive layer [2] and the use of color filters [3]. Furthermore, employing color filters in image sensor can raise additional drawbacks such as absorption of photons by the color filter itself, which limits photocurrent conversion efficiency, additional fabrication, and an installation process which increases production cost. Therefore, it is essential to develop image sensors using better semiconductor materials than conventional Si.

In this regard, organic semiconductors with high absorption coefficients [4-8], and possible wavelength selectivity [9-14], are well suited for such color filter-free image sensor applications. Therefore, in this thesis, I will suggest three different approaches to realize high-performance organic semiconductor-based color filter-free photodiodes; 1) work function tuning approach using polyelectrolytes, 2) Schottky junction approach using color-selective donors, and 3) etalon-electrode approach with a single photoactive layer. By utilizing the approaches, high-performance organic photodiode-based image sensor could be realized and star-shaped full-color image was successfully captured.

2 Approaches for Junction Engineering

2.1 Work function tuning approach using polyelectrolytes

2.1.1 Introduction

Organic semiconductor-based optoelectronic devices, such as organic photovoltaics (OPVs), organic light-emitting diodes (OLEDs), and organic photodiodes (OPDs), have become pivotal elements to replace their inorganic counterparts because of their flexibility, large area, and low-cost processability [15-17]. Because all of these optoelectronic devices are based on diode structures consisting of sequential deposition of various metal, semiconductor, and interfacial layers, smart device engineering to tune the diode characteristics could dramatically enhance the optoelectronic performance [18-20]. Especially, in the case of OPDs, in which both photocurrent and dark current are figures-of-merit of the devices, interface engineering to suppress dark current while maximizing photocurrent has been regarded as an indispensable research objective. In this context, tuning the electrode work function (WF) by insertion of an interfacial layer has been widely studied to improve selective charge collection of OPDs; for example, in the case of a hole-collecting electrode, an interfacial layer can promote hole extraction while blocking electron injection. Typically, metal oxides such as ZnO, TiO_x, or MoO₃ have shown outstanding performance when used as such charge-selection layers [21-23].

To improve the charge selectivity of the interfacial layer, one can consider 1) forming an energy cascade between the active layer and the corresponding electrode to facilitate the photocurrent and 2) increasing the energy barrier against the dark current. For example, to enhance the charge selectivity of the ITO/ZnO electrode of an inverted diode, electron collection can be improved by shifting the conduction band minimum (CBM) of the ZnO layer to the position between the WF of ITO and the lowest unoccupied molecular orbital (LUMO) of the acceptor material. On the other hand, shifting the valence band maximum (VBM) of the ZnO layer deeper can also

enhance the charge selectivity of ITO, by hampering the hole-injection from ITO to the active layer. This implies that fine tuning of both CBM and VBM of the interfacial layer is crucial for enhancing the charge selectivity of the electrode and hence the photodetector performance.

Among various functional materials that can be used for interfacial layers, polyelectrolytes with the ability of forming dipole layers can be promising candidates for a highly efficient charge-selection layer [24,25]. Because polyelectrolytes have organic surfaces, they enable organic–organic junctions when introduced between an electrode and semiconductor. Furthermore, unlike the case of inorganic oxides, they can be easily formed via a solution process at low temperature. With these factors in mind, in this study, we strategically introduced poly(styrenesulfonate) (PSS) as a cathode interlayer of an inverted diode architecture to minimize dark current while preserving optimal photocurrent. Poly[4,8-bis(5-(2-ethylhexyl)thiophen-2-yl)benzo [1,2-b;4,5-b']dithiophene-2,6-diyl-alt-(4-(2-ethyl hexyl)-3-fluorothieno[3,4-b]thiophene-)-2-carboxylate-2-6-diyl)] (PTB7-Th) and [6,6]-phenyl-C₇₁-butyric acid methyl ester (PC₇₁BM) were used as electron donor and acceptor, respectively, of the active layer. The fabricated OPDs were systematically investigated with respect to optical, photophysical and electrical properties. By introducing a PSS interlayer, the dark current in the reverse bias region was efficiently suppressed down to 28 nA/cm² at –5 V without deteriorating the photocurrent, which led to a high detectivity of up to 3.3×10^{12} Jones.

2.1.2 Experimental details

Materials PTB7-Th and PC₇₁BM were purchased from Solarmer and Nano-C, respectively, and used without further purification. Prior to fabrication of OPDs, ITO-patterned glass substrates were cleaned with detergent, distilled water, acetone, and isopropanol by sequential sonication. Sol-gel based ZnO solution was then spin-coated onto the cleaned substrates with a nominal thickness of 40 nm. ZnO solution was prepared by adding 1 g of zinc acetate dihydrate and 0.28 g of ethanolamine in 2-methoxyethanol and stirred at 600 rpm in advance. After the deposition of ZnO films, the substrates were annealed at 200 °C for 30 min. Aqueous PSS solutions were spin-coated onto the ZnO films and annealed at 150 °C for 60 min. Blend solution for active layer deposition was prepared by adding 24 mg of PTB7-Th and 36 mg of PC₇₁BM in 1 ml of chloro-benzene and stirring at 60 °C over 8 h. The blend solution was spin-coated onto the ZnO or PSS thin film and annealed at 80 °C for 10 min. MoO₃ and Au electrode were deposited sequentially through shadow masks by thermal evaporation.

Current density-voltage (J - V) characteristics were measured by Keithley 2400 sourcemeter and Oriel Cornerstone 130 1/8m monochromator, and 652 nm red lasers were used as light sources for photocurrent measurements. Noise current data were collected by using a Stanford Research SR830 lock-in amplifier, and measured noise currents were normalized by the input bandwidth. All measurements were conducted in an N₂-filled glove box, except for LDRs and stability measurements, which were conducted in air. Ultraviolet photoelectron spectroscopy (UPS) data were collected in the 4D beamline at the Pohang Accelerator Laboratory, Korea.

2.1.3 Results and discussion

2.1.3.1 Anionic polyelectrolyte as a cathode interlayer

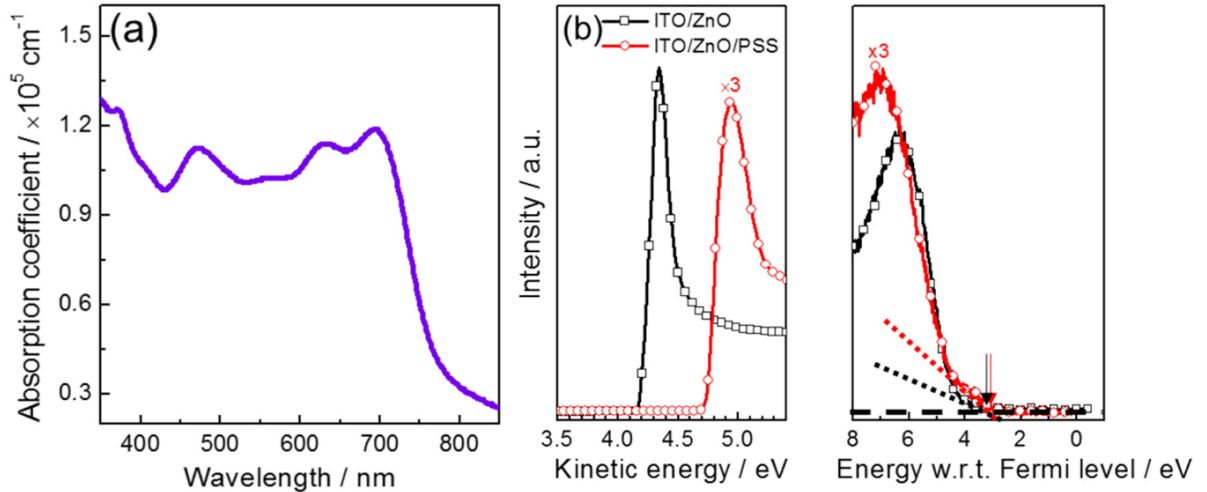


Figure 2.1.1 (a) UV-Vis. spectrum of the PTB7-Th:PC₇₁BM blend film and (b) the UPS spectra of the ITO/ZnO and ITO/ZnO/PSS samples. The arrows in right panel represent the work function-to-valence band maximum distance.

We measured the UV-Vis spectrum of the blend film to elucidate its absorption range. Figure 2.1.1(a) shows the UV-Vis spectrum of the PTB7-Th:PC₇₁BM blend film. High absorption coefficients ($>1.0 \times 10^5 \text{ cm}^{-1}$) are clearly observed for the entire visible region (400–700 nm), and it guarantees high absorption percentage over 98% at a thinner active layer thickness ($\sim 400 \text{ nm}$) than that of Si-based inorganic photodetectors (typically, $\sim 3 \mu\text{m}$) [26]. Therefore, the PTB7-Th:PC₇₁BM blend is suitable for spectrally broadband OPD applications.

To investigate the effect of PSS on the WF of the ITO/ZnO electrode photophysically, UPS analyses were conducted in ultra-high vacuum conditions. As seen in Figure 2.1.1(b), the WF of ITO/ZnO was shifted from 4.19 to 4.73 eV in the secondary cut-off region, without changing the

position of the Fermi level with respect to the valence band maximum in the UPS region. This can be attributed to the formation of an interfacial dipole between the active layer and electrode caused by the insertion of the PSS layer. The sulfonate groups in PSS have negative charges, and they avoid the negatively charged terminal oxygen ions of the ZnO surface. Therefore, an interfacial dipole is formed from the electrode toward the active layer. Since the WF of the ITO/ZnO electrode was lowered, the hole-injection barrier from ITO to ZnO becomes much larger, from 2.23 to 2.77 eV, leading to the enhancement of the hole-blocking property of the ZnO layer. At the same time, because the cascade energy structure for electron extraction between the electrode and semiconductor is still maintained, one can expect a similar photocurrent level after the introduction of the PSS interlayer.

OPDs were fabricated with inverted device geometry (ITO/ZnO/none or with PSS/PTB7-Th:PC₇₁BM/MoO₃/Au) and MoO₃ was used as an anode interlayer.

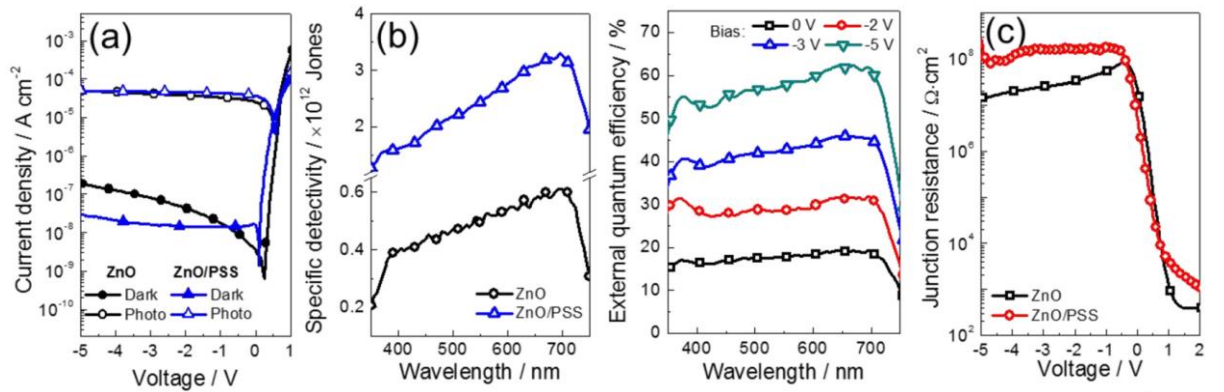


Figure 2.1.2 (a) J - V characteristics in dark and illuminated (AM 1.5 G, $1.8 \times 10^{-4} \text{ W/cm}^2$) circumstances, (b) (left panel) the specific detectivity plots under -5 V and (right panel) external quantum efficiency plots of the optimized devices under various biases as a function of wavelength, and (c) the junction resistance plots as a function of applied voltage.

The thickness of the PSS layer was varied from ~5 nm to ~20 nm and it was found that the thickness of ~10 nm is optimal for both dark current and photocurrent. The J - V characteristics of the fabricated OPDs are displayed in Figure 2.1.2(a). It is clearly seen that the dark current was efficiently suppressed from 1.89×10^{-7} A/cm² to 2.98×10^{-8} A/cm² under -5 V bias, presumably due to the aforementioned shift in the WF. According to the thermionic emission model, dark current can be expressed as a function of the energy barrier height as:

$$J = AT^2 \exp\left(-\frac{q\phi_B}{kT}\right) \quad (\text{Equation 2.1.1})$$

, where A is the pre-exponential factor, q is the elementary charge, ϕ_B is the energy barrier height, k is the Boltzmann constant, and T is the temperature [27]. Therefore, one can see that the enlarged hole-injection barrier (ϕ_B) effectively blocks hole injection from ITO to ZnO, and it leads to the reduction of dark current under the reverse saturation regime. Moreover, in the case of the ZnO/PSS-device, the shape of the semi-log curve is flatter than that of ZnO under the reverse saturation regime. The flat curve in the reverse bias region implies that the tunneling current at the electrode/active layer interface is dramatically reduced [28,29], and this suppressed tunneling current can be attributed to the enlarged hole-injection energy barrier [30]. It is also worthwhile to note that the photocurrent of the ZnO/PSS device is similar to that of the ZnO device, presumably owing to a well-conserved cascade energy structure for electron extraction.

The specific detectivity (D^*), which is known as the figure-of-merit of OPD performance, was obtained via the following equation:

$$D^* = \frac{q\lambda\sqrt{A} \cdot EQE}{hci_n} \quad (\text{Equation 2.1.2})$$

where λ is the wavelength, A is the active area (0.09 cm^2), EQE is the external quantum efficiency, h is the Planck's constant, c is the speed of light, and i_n is the noise current [31]. Figure 2.1.2(b) shows plots of the calculated D^* vs. wavelength. It is noted that the suppression of dark current without sacrificing the photocurrent effectively enhances D^* from 6.12×10^{11} Jones for the ZnO-only device to 3.31×10^{12} Jones for the ZnO/PSS device at 690 nm.

To investigate the shunt resistance (R_{sh}), we calculated the junction resistance (R_j) from the measured dark J – V characteristics data by using the equation:

$$R_j = \frac{\partial V}{\partial J} \quad (\text{Equation 2.1.3})$$

, as seen in Figure 2.1.2(c). Interestingly, R_{sh} was increased by a factor greater than two from $8.25 \times 10^8 \Omega \cdot \text{cm}^2$ to $1.78 \times 10^9 \Omega \cdot \text{cm}^2$, by applying the PSS interlayer. In light of the facts that the interfacial morphology is closely related to R_{sh} , and that R_{sh} increases as the electrode/active layer interfacial morphology improves [32], it is speculated that PSS may also facilitate more favorable interfacial morphology between the ZnO and active layers.

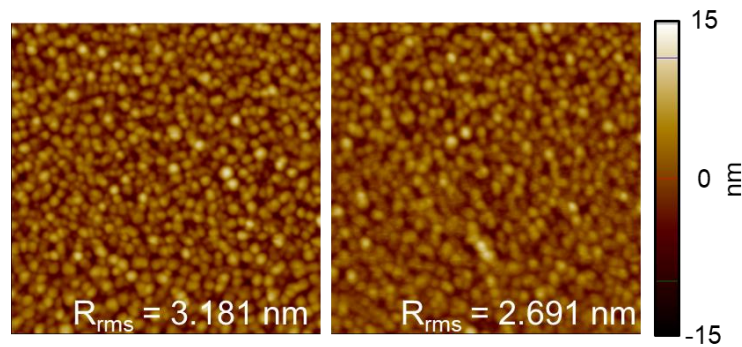


Figure 2.1.3 The atomic force microscope (AFM) topography images of the devices (left panel) without and (right panel) with PSS interlayer ($5 \mu\text{m} \times 5 \mu\text{m}$).

To observe the effect of PSS on the ZnO/active layer interfacial morphology, we studied surface topography images of the active layer by means of atomic force microscopy (AFM). As seen in Figure 2.1.3, the active layer of PSS interlayer-added samples shows not only reduced root-mean-square roughness (R_{rms}) values, but also smoothened and featureless morphology. It implies that the PSS interlayer facilitates more favorable interfacial morphology between the ZnO and active layers, and the resulting smooth interfacial morphology can lead to a decrease of interfacial traps density. Because the presence of trap sites with unexpected energy level can contribute to the dark current, the insertion of PSS can suppress the dark current of the photodiode. Actually, without PSS interlayer, the voltage corresponding to the lowest dark current of photodiode ($V_{\text{oc,d}}$) was found as ~ 0.25 V, which is unusual for photodiode as seen in Figure 2.1.2(a). However, as a result of the insertion of PSS interlayer, $V_{\text{oc,d}}$ shifted to 0 V which can be also related with the decreased interfacial trap density.

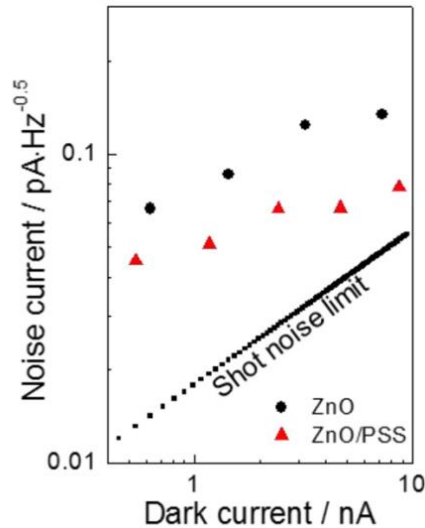


Figure 2.1.4 The noise current distribution of the optimized OPD as a function of dark current.

Noise currents under various dark current values were collected to investigate the effect of the PSS interlayer on total noise current. Although there are many noise current sources such as shot noise, thermal noise, and $1/f$ noise, shot noise is the dominant noise source in total noise calculations in many cases. Therefore, suppressing the dark current can correspond to reducing the noise current. In this regard, a substantial change in total noise current values should be induced by the insertion of a PSS interlayer, which is confirmed by the result shown in Figure 2.1.4. As expected, it is clearly shown that noise current values decrease in the entire dark current range after the introduction of a PSS interlayer. Moreover, the total noise current values seem to be close to the shot noise limit, which implies that the dark current is the main dominant noise source of the fabricated PDs.

We calculated the ideality factor from dark J – V characteristics data by using the simple diode equation:

$$J \approx \exp\left(\frac{qV}{\eta kT}\right) \quad (\text{Equation 2.1.4})$$

, where η is the ideality factor and T is the absolute temperature [27]. The ideality factor is equal to 1 when the recombination–generation current in the depletion region is insignificant and the total current is dominated by the ideal diffusion current; on the other hand, it will be larger than 1 when the total current is dominated by the recombination current.

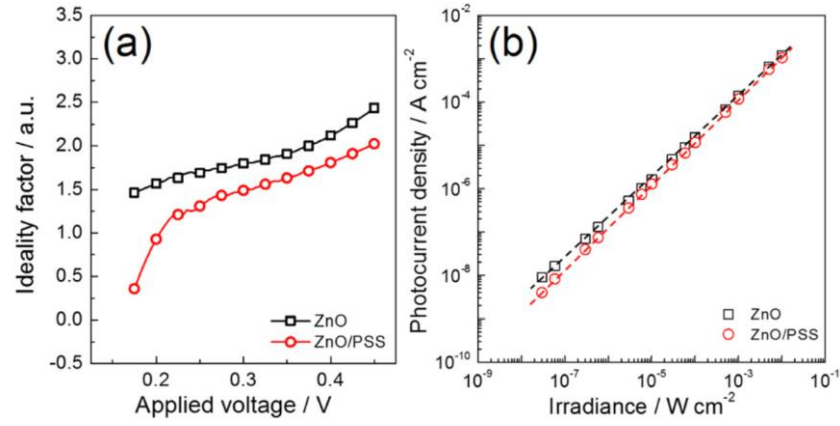


Figure 2.1.5 (a) The ideality factor as a function of applied voltage and (b) linear dynamic range plots at -5 V.

It is known that the ideality factor for real photodiodes typically has a value between 1 and 2. As seen in Figure 2.1.5(a), ZnO/PSS devices have smaller η than ZnO-only devices in the whole forward-bias voltage range. This can be interpreted as the ZnO/PSS-based devices have decreased interfacial trap-assisted trapping and recombination compared to the case of the ZnO-only devices [33,34], which is attributed to the elimination of interfacial traps by the PSS interlayer, and which shows good agreement with the AFM analysis.

LDRs were measured by obtaining the photocurrent under modulated illumination from a laser and monochromator with various neutral-density filters. The LDR is the range over which responsivity is constant. The measured LDR is shown in Figure 2.1.5(b), and the LDR values were 5.1 orders of magnitude for ZnO-only and 5.4 orders of magnitude for ZnO/PSS devices. However, the minimum irradiance of the incident light was only as low as 2.98×10^{-8} W/cm 2 because of our instrument limitations, and this may have led to the low LDR values. Theoretically, the lower limit of the LDR is known as the noise current [1], and J. Huang et al. reported that the

minimum detectable light intensity was very close to the calculated noise equivalent power of photodiodes [35]. Considering the abovementioned circumstances, the minimum detectable light intensities in our system were $4.59 \times 10^{-10} \text{ W/cm}^2$ for the ZnO-only devices and $4.42 \times 10^{-11} \text{ W/cm}^2$ for the ZnO/PSS devices. Therefore, theoretically, the LDR values could be estimated as 6.78 and 8.17 orders of magnitude for the ZnO-only and ZnO/PSS devices, respectively. In the case of the ZnO/PSS devices, the LDR value surpasses or is comparable with that of many inorganic photodetectors, such as GaN (5 orders of magnitude), InGaAs (6.6 orders of magnitude), GaP (11 orders of magnitude), GaAsP (11 orders of magnitude), and Si-based photodetectors (12 orders of magnitude) [35,36]. In addition, the slopes of the fitted lines in Figure 2.1.5(b) were 0.925 and 0.978 for the ZnO-only and ZnO/PSS devices, respectively. A slope value close to unity indicates the reduction of charge recombination and that the fabricated photodiodes are close to ideal photodiodes.

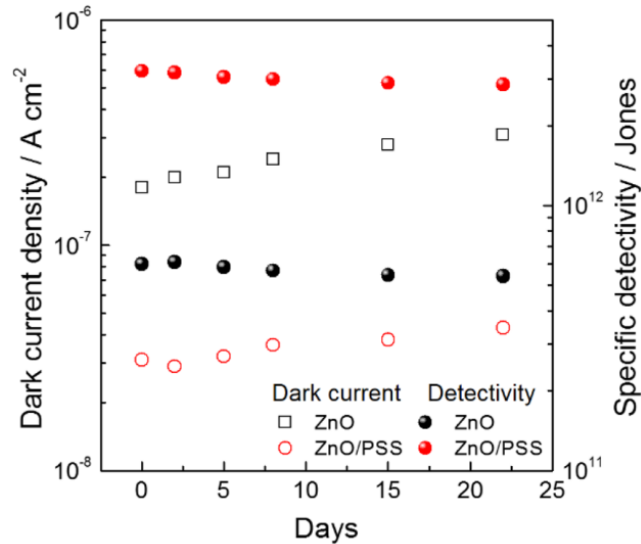


Figure 2.1.6 Stability study of the dark current and specific detectivity with different interlayer. The dark current and detectivity data were collected at the bias of -5 V.

Lastly, we measured the time dependent dark currents and specific detectivities of the fabricated photodiodes to conduct a stability test. The samples were stored in the ambient environment and in a dark place. As can be seen in Figure 2.1.6, the specific detectivity remains almost constant in both cases. However, the dark current values deteriorated slightly after 22 days, from $1.89 \times 10^{-7} \text{ A/cm}^2$ to $3.12 \times 10^{-7} \text{ A/cm}^2$ for the ZnO-only devices and from $2.98 \times 10^{-8} \text{ A/cm}^2$ to $4.34 \times 10^{-8} \text{ A/cm}^2$ for the ZnO/PSS photodiodes, which are similar trends.

2.1.3.2 Conjugated polyelectrolytes as cathode interlayers

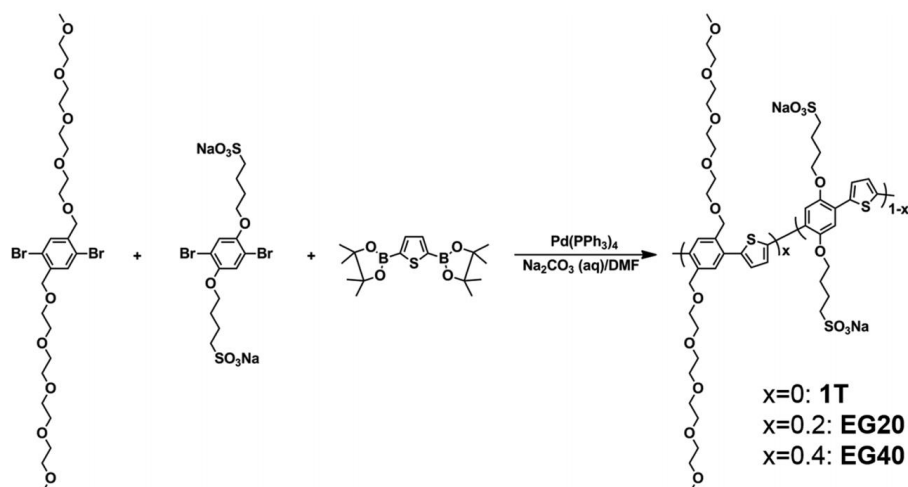


Figure 2.1.7 Chemical Structures and Synthetic Schemes of conjugated polyelectrolytes (CPEs).

As shown in Figure 2.1.7, we synthesized a homopolymer of 1T and two random copolymers via a Suzuki coupling reactions of a thiophene diborate compound with different molar feed ratios of dibromo 1,4-bis(4-sulfonatobutoxy)benzene (SPh) and dibromo 1,4-bis(4-tetraethylene glycol)benzene (EGPh) for polymerization (SPh:EGPh was 0.8:0.2 for EG20; 0.6:0.4 for EG40). 1T was synthesized according to a reported procedure [37].

Figure 2.1.8(a) shows the UV-Vis absorption spectra of the CPEs in solution phase with different composition ratios. Regardless of the composition ratios, all the CPEs showed a characteristic absorption peak at 413 nm, which corresponds to the π - π transition. At the same time, a very weak absorption feature at 600–800 nm, which can be assigned to a radical cation (or polaron), tends to decrease as the EG content increases. Therefore, it is expected that the polaron generation

decreases with the increase in EG content, as supported by electron spin resonance analysis (Figure S1).

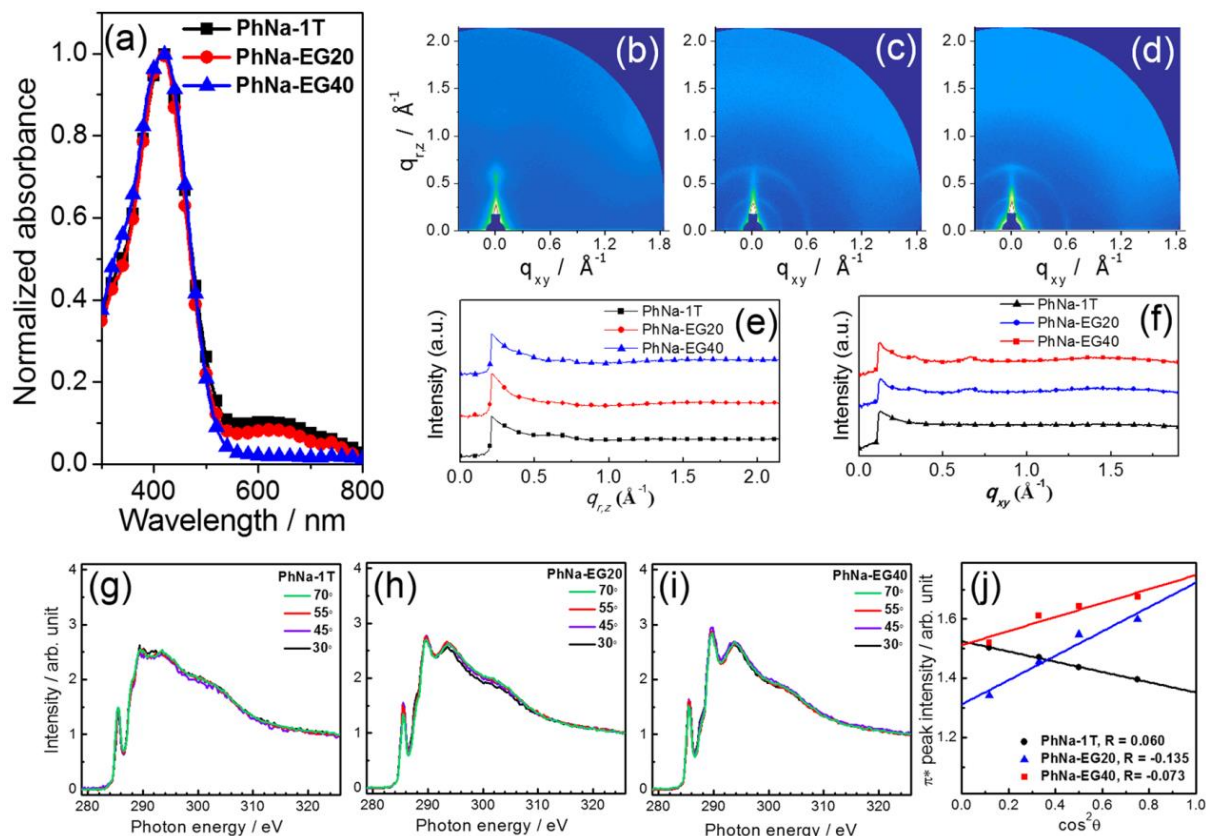


Figure 2.1.8 (a) Absorption spectra of CPEs in aqueous solutions. (b–d) GIXD patterns of thin films of (b) 1T, (c) EG20, and (d) EG40. (e) Out-of-plane and (f) in-plane line-cut data corresponding to (b–d). (g–i) NEXAFS data measured under various incident light angles of thin films of (g) 1T, (h) EG20, and (i) EG40. (j) π^* transition intensities versus incidence angle. Solid lines represent the fitted curves.

2D-GIXD measurements were performed in order to investigate the effect of chemical structural change of the CPEs on the polymer packing properties in a film, and the results are summarized in Figures 2.1.8(b)–(f). Notably, EG20 and EG40 show (100) Bragg diffraction peaks with series up to (200) , indicating the formation of lamellar crystalline domains, while 1T (without the EG

moiety) shows nearly featureless scattering patterns. The measured inter-lamellar distance of EG40 based on the (100) diffraction peak is ~ 1.90 nm, which is typical of conjugated polymers considering the length of the ethylene glycol side chains [38]. It seems that the charged end groups of the SPh moiety prohibits intermolecular lamellar stacking of 1T, while the increased proportions of ethylene glycol side chains in EG20 and EG40 enables partial lamellar stacking. The crystalline orientation of the CPEs were further investigated by means of near edge X-ray absorption fine structure (NEXAFS) spectroscopy as summarized in Figures 2.1.8(g)–(i). In these spectra, the features at ~ 285.3 , 287–291, and 292–307 eV can be assigned to the π^* (C=C), σ^* (C–S), and the π^* (C=O) orbitals mixed with Rydberg orbitals and several σ^* orbitals, respectively [37]. In particular, by analyzing the incident light angle dependencies of the π^* (C=C) orbital peak intensities, we can calculate the dichroic ratio (R) as summarized in Figure 2.1.8(j). The R values of EG20 and EG40 are negative while that of 1T is positive, implying that EG20 and EG40 exist in preferential face-on orientations, while 1T preferentially exists in the edge-on orientation. In conjugated polymers, more developed lamellar stacking is very often related to a higher charge carrier mobility. In addition, in vertical device structures, the face-on orientation is more beneficial for charge transport when compared to the edge-on orientation. It is widely reported that polymers having preferential face-on orientation positively affect the power conversion efficiency when they are used as photoactive materials for OPVs [39–42]. Therefore, EG20 and EG40 can potentially lead to a more efficient charge extraction when applied as an interface layer of OPDs.

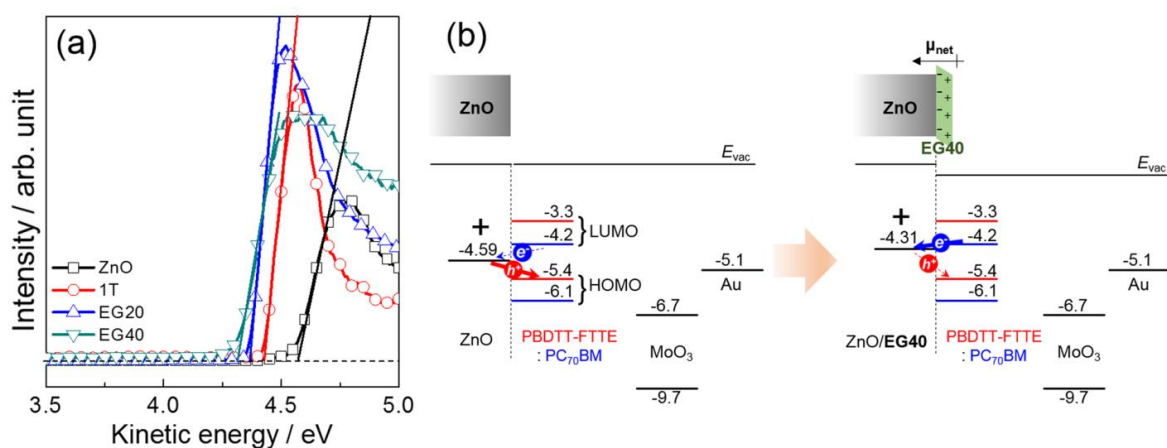


Figure 2.1.9 (a) Secondary cutoff region of UPS to show a work function shift as a result of the introduction of CPEs and (b) schematic energy level diagram to highlight the effect of CPEs for efficient hole blocking at the ZnO/PTB7-Th:PC₇₁BM interface of inverted OPDs operating under reverse bias mode.

Figure 2.1.9(a) shows the secondary cutoff region of the spectra obtained by UPS for 1T, EG20, and EG40 layers (~10 nm) deposited onto ZnO films. It is evident that the WF of ZnO is shifted to a lower value of kinetic energy as the EG content increases in the copolymer. Such a decrease of WF of ZnO with the introduction of thin layers of CPE can be attributed to the formation of molecular and interface dipoles [43]. The negative charges of the sulfonate groups of the synthesized CPEs make them preferentially adsorbed onto the positively charged terminal zinc ions of the ZnO surface. Therefore, an interfacial dipole is formed from the active layer toward the electrode, resulting in decreased WF of ZnO. Moreover, the high electron density of the ethylene

glycol moiety can passivate the surface traps of ZnO [44], resulting in decreased WFs. It is possible that the highly organized polymer chains of EG20 and EG40 in the films, as demonstrated by GIXD studies, are favorable for maximizing the molecular dipoles, resulting in a higher degree of energy level shifts compared to 1T. This is very useful for reducing the dark current in inverse-structured OPDs, as schematically described in Figure 2.1.9(b). Considering that the photodiodes are operated under reverse bias, dark currents can be generated by hole injection from ITO/ZnO to the highest occupied molecular orbital (HOMO) of donor materials. As seen in the Figure 2.1.9(b), the energy gap ($\Delta\phi$) for hole-injection increased from 0.81 to 1.09 eV as a result of CPEs insertion. According to the thermionic emission model, dark current under reverse bias mode can be considered as a function of energy barrier height Equation 2.1.1. Therefore, the increase of energy barrier height leads to the suppression of the dark current of the photodiode. In addition, after the changes in the energy levels, the CPE-coated ZnO forms a near-ohmic contact with the LUMO levels of the acceptor material. Therefore, the introduction of EG20 and EG40 can potentially decrease the dark current and improve the photocurrent in the OPDs.

To investigate the effect of the CPE interlayer on the OPD performance, we fabricated a bulk heterojunction-based OPD with PTB7-Th as the electron donor and PC₇₁BM as the electron

acceptor. An inverted OPD structure was constructed by using ZnO as the electron transport/hole blocking layer and MoO₃ as the hole transport layer. The aqueous 1T, EG20, and EG40 solutions were spin-coated onto the ZnO layer. The PTB7-Th: PC₇₁BM blend dissolved in chlorobenzene was spin-coated to form the active layer with a nominal thickness of 390 nm, which was the optimized thickness in our system. Because of the selective solubility of the CPEs in water, chlorobenzene used for the active layer deposition could be a near-ideal orthogonal solvent, without causing any significant damage to the pre-formed CPE layer.

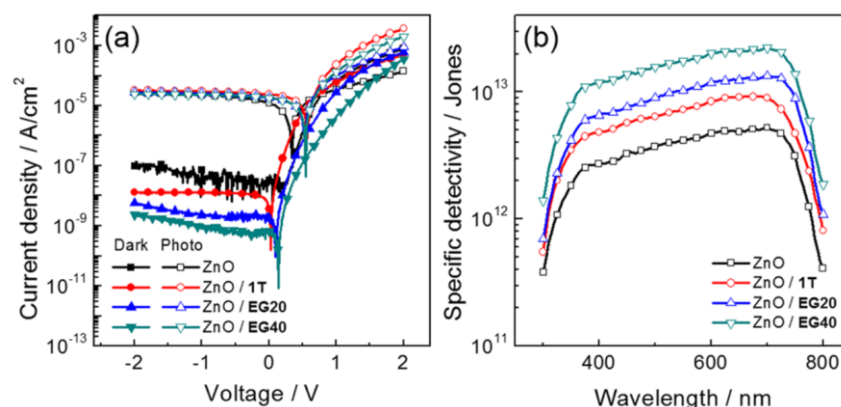


Figure 2.1.10 (a) Dark current and photocurrent curves with various interlayers (1T, EG20, and EG40). The light intensity used was 36.5 $\mu\text{W}/\text{cm}^2$. (b) Calculated specific detectivity as a function of wavelength under -2 V bias.

Figure 2.1.10(a) shows the current density-voltage (J - V) characteristics with various CPE layers. The dark current values reduced dramatically from 97.3 nA/cm² for ZnO to 2.4 nA/cm² for ZnO/EG40 at -2 V, accompanied simultaneously by a slight increase in photocurrent. As

mentioned above, the decreased WF of the ITO/ZnO electrode can hamper the hole injection from ITO to HOMO of the donor material, resulting in the suppression of the dark current. At the same time, the near-ohmic contact for electrons enhances the photocurrent. Besides, we observed that the dark J - V curves in reverse bias region become more flattened after inserting the CPEs. The flattened dark J - V curves imply that the tunneling current between the interlayer and the active layer was dramatically suppressed [29] and it is widely known that the main source of the tunneling current is the surface traps [45]. Therefore, the insertion of CPEs resulted in not only decreasing the WF, but also suppressing the tunneling-induced dark current.

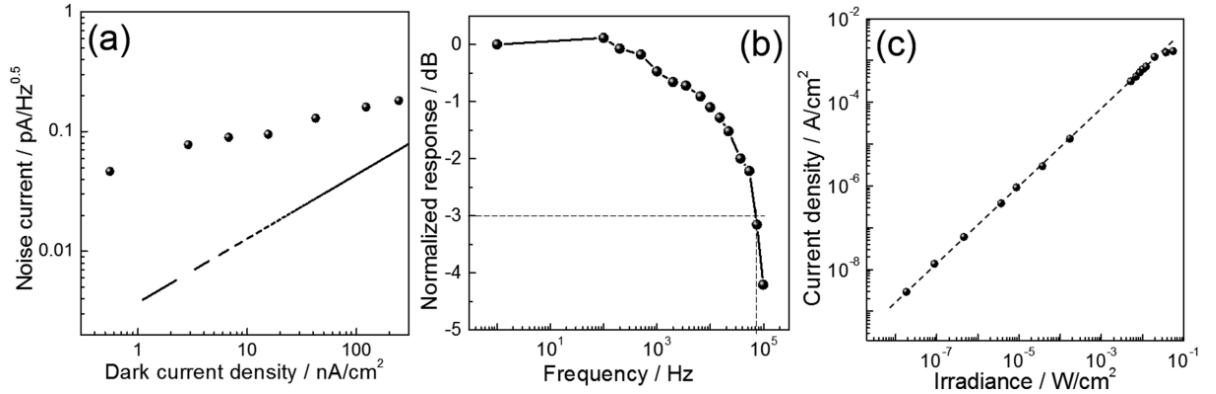


Figure 2.1.11 (a) Measured noise current, (b) response plot as a function of switching frequency of light, and (c) linear dynamic range of the fabricated OPDs with EG40 as an interlayer. In (b) and (c), the measured bias was -2 V.

To measure the specific detectivity more precisely, we carried out the noise current measurements to analyze the actual noise in the fabricated devices. The results for EG40 are shown in Figure 2.1.11(a) and the shot noise limit is also displayed for comparison. The measured noise

current was just above ~ 2 – 3 times of the shot noise limit calculated from the dark current, implying that the shot noise and thus dark current are the main source of noise in the fabricated OPDs. As summarized in Figure 2.1.10(b), the calculated D^* values of OPDs with **EG40** reached over 10^{13} Jones for the entire visible range (400–700 nm), which is comparable to Si-based inorganic photodiodes [46] and these results are comparable to the results reported as high-performance OPDs (Table 2.1.1) [20,47,48].

	Dark current density (nA/cm ²)	Responsivity (A/W)	EQE (%)	D^* ($\times 10^{13}$ Jones)
Ref. 20	~ 20 @ -2 V	~ 0.3 @ ~ 640 nm, -2 V	~ 67 @ ~ 360 nm, -2 V	0.1 @ 630 nm, -1 V
Ref. 47	7.72 @ -1.5 V	0.24 @ 546 nm, -1.5 V	60 @ -1.5 V	0.48 @ 546 nm, -1.5 V
Ref. 48	~ 100 @ -2 V	0.18 @ 690 nm, -0.1 V	33 @ 600 nm, -0.1 V	2.5 @ 690 nm, -0.1 V
This work	2.4 @ -2 V	0.53 @ 700 nm, -2 V	69.7 @ 670 nm, -2 V	2.1 @ 700 nm, -2 V

Table 2.1.1 Comparison of figures-of-merit for OPDs reported recently.

Fast response time against incident light is one of the most important performance criteria for OPDs. We observed that the responsivity of the OPD decreases as a function of increasing switching frequency of the incident light by a combination of oscilloscope, laser diode, and function generator, as seen in Figure 2.1.11(b). The calculated -3 dB frequency was ~ 72 kHz, which is sufficiently high for image sensing applications and comparable with inorganic photodiodes such

as GaN or GaAsP photodiode [36,49]. The -3 dB frequency ($f_{-3\text{dB}}$) can be calculated by the equation:

$$\frac{1}{f_{-3\text{dB}}^2} = \frac{1}{f_{-3\text{dB,RC}}^2} + \frac{1}{f_{-3\text{dB,t}}^2} \quad (\text{Equation 2.1.5})$$

, where $f_{-3\text{dB,RC}}$ and $f_{-3\text{dB,t}}$ are the RC-limited and transit-time limited -3 dB frequency, respectively [1]. From the dark J - V curve and geometric capacitance calculation [47], the series resistance and the capacitance of the optimized device were found as $453 \Omega \cdot \text{cm}^2$ and 4.3 nF/cm^2 , respectively, which correspond to 81.5 kHz of $f_{-3\text{dB,RC}}$. Because this value of $f_{-3\text{dB,RC}}$ is nearly similar to the actually measured $f_{-3\text{dB}}$, it can be said that the temporal response of the photodiode is limited by RC time, which corresponds to the response time of $\sim 7.74 \mu\text{s}$.

Finally, we measured the LDR, which is another figure-of-merit for PDs. LDR is the range of intensity of the incident light that responsivity maintains constant [35]. The measurements were conducted with the abovementioned laser diode and the modulation frequency was 35 Hz . As seen in Figure 2.1.11(c), the measured LDR was 110 dB , corresponding to 5.5 orders of magnitude. Here LDR was obtained by

$$\text{LDR} = 20 \log_{10} \left(\frac{j_{\max}}{j_{\min}} \right) \quad (\text{Equation 2.1.6})$$

, where j_{\max} and j_{\min} are maximum and minimum detectable current density, respectively [1].

The obtained LDR value is slightly smaller than the highest values reported recently [31,35,36,50,51], however, it can be attributed to the fact that our instruments and the neutral density filter limit the minimum irradiance to 18.5 nW/cm^2 . Theoretically, the lower limit of the LDR is determined by the noise current [52] and according to this theory, the estimated LDR will be over 170 dB, corresponding to 8.5 orders of magnitude. Besides, the measured slope of LDR was close to unity (0.95) implying that the fabricated OPD was a nearly ideal without any unexpected charge recombination or charge traps.

2.2 Schottky junction approach using color-selective donors

2.2.1 Introduction

Over the last decade, image sensor technologies have been continuously researched to increase the number of pixels. As a result, new integration technologies have dramatically improved the resolution of the image sensor [53]. Nonetheless, to further improve image quality, it is necessary to extend the dynamic range, improve sensitivity, and prevent crosstalk or signal mixing between pixels.

In this regard, the conventional Si CMOS image sensors suffer from fundamental limitations: 1) a low absorption coefficient and resulting thick active layer [54], 2) panchromatic absorption [1], and 3) high temperature fabrication process [55]. Interestingly, organic image sensors using OPDs have a great potential to overcome all the drawbacks of Si CMOS devices so that the resolution of the image sensor can be further improved. Unlike the indirect band gap of Si, organic semiconductors follow a direct band gap light absorption process; thus, the absorption coefficient is almost three orders of magnitude higher than that for Si [56]. Therefore, the active layer of OPDs can be much thinner (as low as hundreds of nanometers) than that using Si ($>3\ \mu\text{m}$) [2]. This is particularly important because shorter illumination pathways within the image sensor can be guaranteed in OPD, which can prevent crosstalk or signal mixing between pixels [57]. In addition, organic semiconductors possess the potential for wavelength selectivity via molecular design/synthesis, enabling multicolor imaging of the image sensor without the use of color filters. Eliminating expensive color filters from the image sensor impact greatly the cost of

manufacturing and the resolution when considering the large spatial requirement for color filter installation as well as their material cost [1]. Furthermore, as with all other types of organic devices, OPDs are compatible with flexible plastic substrates because they do not require high temperature manufacturing processes.

Over the past several years, extensive research on OPDs with color selectivity has been carried out. Most of this research, however, has focused on green-selective OPDs [9,49,58,59], presumably because of the difficulties related to realizing blue- and red-selective absorption of organic semiconductors. Especially for red-selection, a largely delocalized conjugation structure should be introduced into the molecular structure to expand the absorption spectrum of π -conjugated organic compounds to 600 nm or higher. To obtain such a narrow band gap, an alternating donor-acceptor (D-A) strategy is often used to induce strong intramolecular charge transfer (ICT). In this case, two main absorption peaks corresponding to not only ICT (at longer wavelengths) but also π - π^* (at shorter wavelengths) transitions are often observed. Consequently, for many D-A alternating copolymers, it is practically impossible to have the absorption peak only at ~650 nm while suppressing absorption in all other wavelength regions. Therefore, additional optical tuning is required to realize narrow band red-selective OPDs. Armin and coworkers have devised a “charge collection narrowing” mechanism of OPDs, where color-selectivity is produced near the absorption edge of the introduced organic semiconductor bulk heterojunction [31]. This smart method successfully demonstrated narrow-band red-selective OPDs; however, photoactive layer thicknesses above 1 μm were required. One of the most important advantages of OPDs is their

thin photoactive layer, in contrast to that for Si; therefore, the realization of a thin film red-selective photodiode is still a challenging task.

Here, we demonstrate a thin film blue- and red-selective OPDs using poly(1,5-bis(hexyloxy)naphthyl-2,6-diyl)thiophene-2',5'-yl) (PNa6-Th) and poly[(2,5-bis(2-hexyldecyloxy)phenylene)-alt-(5,6-difluoro-4,7-di(thiophen-2-yl)benzo[c][1,2,5]-thiadiazole)] (PPDT2FBT) [60-62], respectively, and ZnO as the photoactive layer.

PNa6-Th was strategically designed to have well-defined blue absorption as well as good charge transport; dialkoxynaphthalene donor was employed for its strong π -stacking, linear planar π -system, and good chemical and thermal stability resulted from deep HOMO level and thiophene donor was used to improve the backbone planarity of the polymer [63]. The synthesized PNa6-Th showed a narrowband absorption with a full width at half-maximum (FWHM) of ~100 nm for blue light (central wavelength ~420 nm). We constructed a Schottky junction structure using ITO/ZnO transparent electrode, together with PNa6-Th to achieve a blue-selective OPD. It is known that a Schottky junction structure is an optimized structure for suppressing dark current because it strictly limits the undesired dark current injection due to Schottky barrier [64]. However, the limited charge generation region (depletion region) compared to that of bulk heterojunction can be a weakness of the Schottky junction structure for efficient exciton dissociation. To overcome this issue, we added [6,6]-phenyl-C₆₁-butyric acid methyl ester (PC₆₁BM) in the PNa6-Th polymer film. PC₆₁BM has high absorption coefficients at blue region (400–500 nm) and low absorption coefficients at the rest of the visible region (500–700 nm) and

therefore, we anticipated that adding a low weight percent of PC₆₁BM would only affect charge generation without damaging the absorption spectrum. By adding an appropriate amount of PC₆₁BM, the PC₆₁BM-added PPD showed a higher EQE compared to pristine devices and it is speculated that the boost in EQE is originated from a synergistic effect of the expansion in charge generation region (PNa6-Th:PC₆₁BM donor–acceptor interfacial area) and the increase of photocurrent due to the formation of percolation pathway.

In the meantime, PPDT2FBT has two absorption bands: the band I at red region with a peak near 650 nm and non-negligible band II absorption near 420 nm [62]. We focused on two parameters to confine the photo-responsive range of the photodiode into the red-selective band I region and to realize efficient charge dissociation, transport, and collection without allowing a dark current injection into the PPDT2FBT-based photodiode: (1) the thickness of PPDT2FBT was carefully optimized to suppress band II absorption and (2) the sol-gel processed ZnO was strategically introduced to function as an electron acceptor layer and optical filter. We optimized the thickness of the PPDT2FBT and ZnO layers by optical simulation based on the transfer matrix method [65,66], by which the unwanted absorption and spectral response at band II could be significantly suppressed.

2.2.2 Experimental details

Materials PNa6-Th was synthesized as described previously [67]. PPDT2FBT was synthesized as described previously [60,61]. Soxhlet extraction was performed for the purification of the synthesized PNa6-Th. Mucosol, zinc acetate dihydrate, ethanolamine, 2-methoxyethanol, molybdenum trioxide, chloroform, and chlorobenzene were purchased from Sigma-Aldrich and used without further purification steps.

Device Fabrication ITO-coated glass substrates were mechanically cleaned with a combination of cotton buds and aqueous Mucosol solution. After cleaning, the substrates were sequentially sonicated in a Mucosol solution, distilled water, acetone, and isopropanol for 15 min each. The substrates were then dried in a nitrogen flow, and the dried substrates were treated by an oxygen plasma for 20 min to create a hydrophilic surface. ZnO films were fabricated according to the sol-gel method [68]. For the sol-gel precursor solution, zinc acetate dihydrate (100 mg) and ethanolamine (28 mg) were mixed with 2-methoxyethanol (1 ml). The solution was stirred at 60 °C for 4 h. Then, the solution was spin-coated onto the plasma-treated substrates at 2000 rpm for 45 s. After precursor solution coating, the substrates were annealed at 250 °C to complete the sol-gel reaction. The nominal thickness of a single ZnO layer was ~40 nm. To make thick (> 40 nm)

ZnO films for red-selective OPD, abovementioned sequence was repeated to achieve a thickness of ~140 nm. For fabricating blue-selective OPD, 20 mg of PNa6-Th was dissolved in 1 mL of chloroform. In case of PC₆₁BM-added solution of 15 wt.%, 20 mg of PNa6-Th and 3 mg of PC₆₁BM were mixed in 1 mL of chloroform. Each solution was stirred at least 4 h for homogeneous mixture. PNa6-Th or PNa6-Th/PC₆₁BM solutions were spin-coated onto the ITO/ZnO substrates and the coated substrates were annealed at 80 °C for 10 min. For the fabrication of red-selective OPD, PPDT2FBT was dissolved in chlorobenzene to make a polymer solution with a concentration of 17 mg/ml, and the solution was spin-coated onto the ZnO-coated substrates. The coated substrates were annealed at 130 °C for 10 min to eliminate excess solvent. MoO₃/Ag electrodes were fabricated by sequential thermal evaporation (MoO₃: 0.5 Å/s, Ag: 1.0~2.0 Å/s).

Device Characterization Dark J - V characteristics were measured using a LabView-controlled Keithley 2400 SourceMeter, and J - V characteristics and the specific detectivity spectrum were measured from the abovementioned instrument with an Oriel Cornerstone 130 1/8 m monochromator. For measuring noise current of the OPDs, we used the Stanford Research SR830 Lock-in Amplifier connected with Keithley 2400 and Newport Chopper Controller (Model number: 75160) for synchronization of frequency. The Lock-in Amplifier was controlled by lab-made

LabView program. For noise current collection, firstly, noise voltage was point-by-point collected by using the abovementioned LabView program. Next, normalized noise current data were calculated by using collected noise voltage, sensitivity of the Lock-in Amplifier and input frequency. The noise current was directly measured using a Stanford Research SR830 Lock-in Amplifier, and the measured noise currents were normalized with respect to the input bandwidth. To perform LDR measurements of the fabricated red- and blue-selective OPDs, two different lasers (650 nm, and 473 nm) were used with various neutral density filters. These light sources were calibrated using commercial Si-photodetectors, and all measurements using the light sources were performed at a light modulation frequency of 35 Hz. All measurements were conducted in a N₂-filled glove box. Optical constants for optical simulation were collected using a V-VASE ellipsometer (J.A. Woollam Co.) or calculated from the reflectance, absorbance, and thickness of the sample [69]. The thickness values of all films stated in this manuscript were measured by DektakXT Stylus Profiler.

Transit Time Calculation Transit time(t_{tr}) for each carrier in a planar heterojunction structure can be calculated by

$$t_{tr}^{holes} = \frac{d}{\mu_h E} \quad (\text{Equation 2.2.1})$$

or

$$t_{tr}^{electrons} = \frac{d}{\mu_e E} \quad (\text{Equation 2.2.2})$$

for the hole and electron, respectively. In Equations 2.2.1 and 2.2.2, d is the thickness of each layer, μ_h and μ_e are the hole and electron mobilities, respectively, and E is the electric field, expressed as according to Equation 2.2.3 [58]:

$$E = \frac{V}{d_{PPDT2FBT} + d_{ZnO}} \quad (\text{Equation 2.2.3})$$

The space-charge limited current method enables the measurement of μ_h and μ_e by fitting the experimental J - V characteristics with the Mott-Gurney equation [70]. The calculated hole and electron mobilities can be found in Table 2.2.1 below.

	PNa6-Th:PC ₆₁ BM (15 wt%)	PPDT2FBT	ZnO
Hole	1.90×10 ⁻⁵	2.01×10 ⁻⁴	-
Electron	2.39×10 ⁻⁶	-	8.68×10 ⁻⁵

Table 2.2.1 Summary of the measured charge carrier mobility values of photoactive layers. The unit of the mobility values is cm²/(V·s).

2.2.3 Results and discussion

2.2.3.1 Introduction of acceptors for enhanced external quantum efficiency

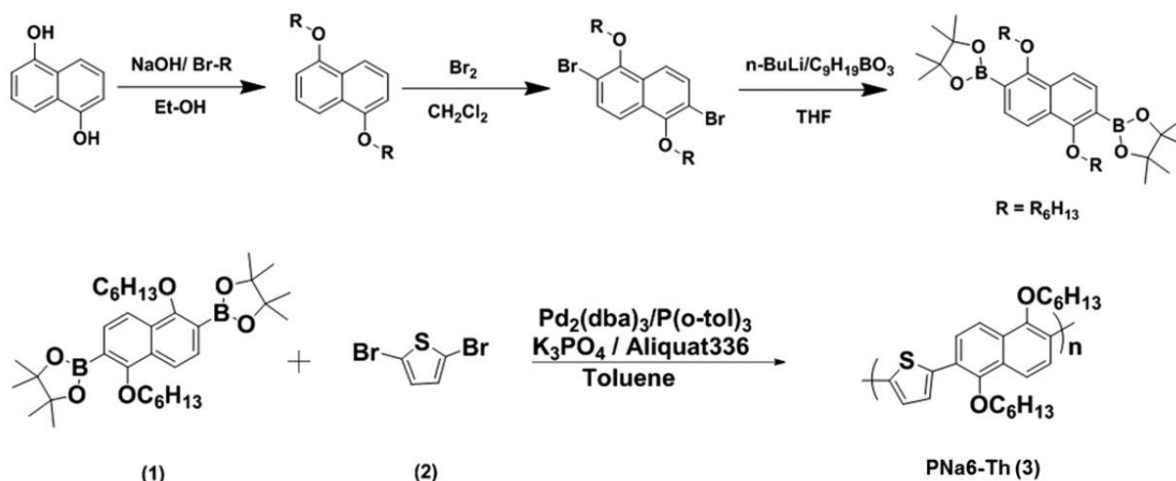


Figure 2.2.1 Synthetic route of PNa6-Th.

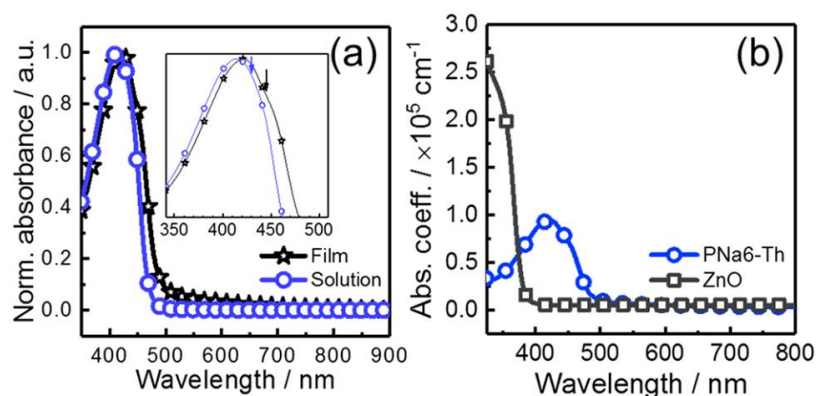


Figure 2.2.2 (a) UV-vis absorption spectra in the solution phase (open circle) and film phase (open star) and (b) the absorption coefficient spectra of PNa6-Th and ZnO films. In the inset of (a), the positions of absorption shoulder are expressed as arrows of corresponding colors.

The synthetic routes for PNa6-Th are depicted in Figure 2.2.1. The polymer was obtained by Suzuki coupling reaction using 2,5-dibromothiophene and dialkoxynaphthalene borate. We investigated the optical properties of the synthesized polymer by measuring its UV-visible absorption spectra (Figure 2.2.2(a)), which displayed absorption peaks at 416 nm (solution) and 426 nm

(film) and absorption shoulders at ~430 nm (solution) and ~445 nm (film). The peaks near 420 nm can be attributed to a π - π^* transition originated from the naphthalene moiety [71] and the absorption shoulders are attributed to intermolecular interaction by π -stacking [72]. In addition, we observed a slightly bathochromic shift of ~10 nm in the film phase, which results from J-aggregation-like molecular packing [59]. The synthesized PNa6-Th exhibited a high absorption coefficient of $9.4 \times 10^4 \text{ cm}^{-1}$ (Figure 2.2.2(b)) and it absorbs sufficient light (>90%) with a thin photoactive layer (~250 nm). The FWHM values extracted from absorption spectra of the synthesized polymer in solution and the film phase were 96 and 100 nm, respectively, which are sufficient narrowband absorptions in the blue wavelength region. We could obtain an optical bandgap, HOMO and LUMO by measuring the absorption onset of the film spectrum and by conducting the cyclic voltammetry measurement (Figure 2.2.3(a)), respectively. The calculated optical bandgap was ~2.52 eV and HOMO and LUMO levels were -5.4 and -2.88 eV, respectively.

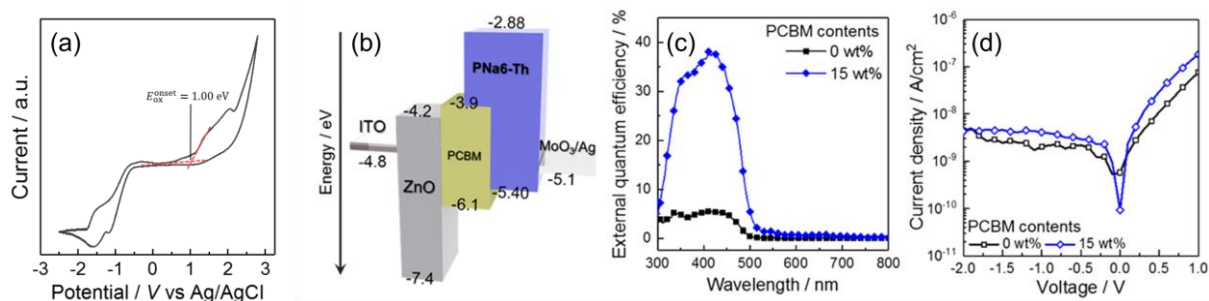


Figure 2.2.3 (a) The cyclic voltammogram of the PNa6-Th. (b) the energy levels of the used materials, (c) the EQE spectra, and (d) dark current density–voltage (J - V) characteristics of various wt. % ratios of PC₆₁BM. In Figure 2.2.3(a), HOMO of the polymer was calculated by the equation: $E_{\text{HOMO}} = -(4.4 + E_{\text{ox,onset}}) [\text{eV}]$.

To measure the device performance, we fabricated a Schottky photodiode using PNa6-Th as the photoactive material with ITO/ZnO transparent electrode. An inverted device geometry was

adopted and MoO_3 was used as a hole-transport layer, as seen in Figure 2.2.3(b). 15 wt.% of PC_{61}BM compared to the mass of PNa6-Th was added on the PNa6-Th solution. The measured EQE spectra can be found in Figure 2.2.3(c). As seen in Figure 2.2.3(c), when the additional PC_{61}BM was not added, very low EQE of 5.4% was observed. By adding 15 wt.% of PC_{61}BM , which is the typical acceptor weight percentage for percolation pathway formation [73], the EQE and photocurrent density were sharply increased. Since the EQE is directly proportional to the generated photocurrent and the percolation pathway leads to the increase of photocurrent, it is speculated that percolation pathway made of PC_{61}BM was formed between PNa6-Th and ZnO when the PC_{61}BM ratio reaches 15 wt.%. However, PC_{61}BM percolation pathway may also occur electron injection from cathode (MoO_3/Ag) by provide more favorable LUMO level to electron at cathode for electron injection, we measured dark current density–voltage (J – V) characteristics to investigate this point. As can be seen in Figure 2.2.3(d), the variation in dark current density is nearly constant until the ratio reaches 15 wt.%. Unlike organic photovoltaics, suppression of dark current is as essential as increase of photocurrent for organic photodiodes to enhance the signal-to-noise ratio. Therefore, we can address that the addition of PC_{61}BM resulted in only an increase of EQE without sacrificing low dark current.

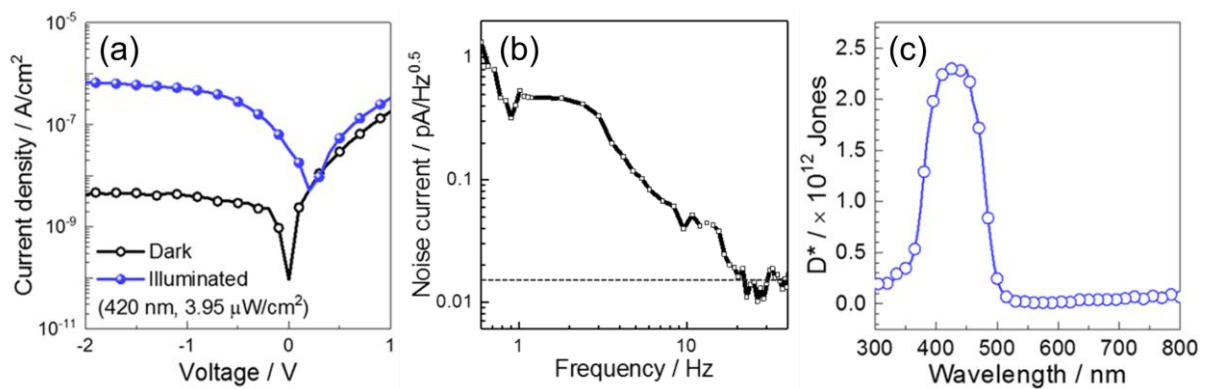


Figure 2.2.4 (a) J - V Characteristics and (b) noise current as a function of modulation frequency, and (c) specific detectivity spectrum of the optimized OPD. Specific detectivity spectrum and noise current were measured at -1 V.

The J - V characteristics of the optimized OPD are depicted in Figure 2.2.4(a). A low dark-current density of 4.1 nA/cm^2 at -1 V was obtained, which is attributed to the introduction of the Schottky junction structure. The specific detectivity (D^*) is one of the figures-of-merit of OPDs and it can be calculated by Equation 2.1.2. We calculated the specific detectivity from EQE values at Figure 2.2.3(c) and noise current displayed at Figure 2.2.4(b) and the calculated specific detectivity is shown at Figure 2.2.4(c). It is clearly shown that a narrowband detection for blue-light occurs with a narrow FWHM of 103 nm . It can be confirmed that the absorption spectrum of donor material (PNa6-Th) is well reflected in the spectral response of the final device without the disturbance of absorption of acceptor materials (PC_{61}BM).

To examine the electrical properties of each constituting layer (PNa6-Th: PC_{61}BM , ZnO), we conducted space charge-limited current (SCLC) mobility measurement [70]. Since it can be assumed that certain charge carrier flows only certain layers for photocurrent generation, that is, photogenerated holes flow only through PNa6-Th: PC_{61}BM layer and photogenerated electrons flow only through ZnO layer, we fabricated hole-/electron-only devices consisting of each layer as the active layer (hole: ITO/PEDOT:PSS/PNa6-Th: PC_{61}BM /MoO₃/Ag, electron: ITO/ZnO/LiF/Al). The measured hole and electron mobilities were $\mu_h = 1.90 \times 10^{-5} \text{ cm}^2/(\text{V}\cdot\text{s})$ and $\mu_e = 2.39 \times 10^{-6} \text{ cm}^2/(\text{V}\cdot\text{s})$, respectively (Table 2.2.1). From the measured thickness information on each active layer components (PNa6-Th: PC_{61}BM = $\sim 320 \text{ nm}$, ZnO: $\sim 40 \text{ nm}$), we can calculate the transit time. The transit time is the time taken for holes or electrons to move from the donor/acceptor interface of photoactive layer to the corresponding electrode. The transit time for each carrier can be calculated using Equation 2.2.1 and Equation 2.2.2. From the equations and parameters, the calculated transit time values for hole and electron are $t_{\text{tr,h}} = 6.03 \times 10^{-5} \text{ s}$ and $t_{\text{tr,e}} = 6.06 \times 10^{-5} \text{ s}$, respectively. Therefore, it can be confirmed that the difference in transit time is small down to few hundreds of nanoseconds. The transient response and LDR are the

other important figures-of-merit of OPDs.

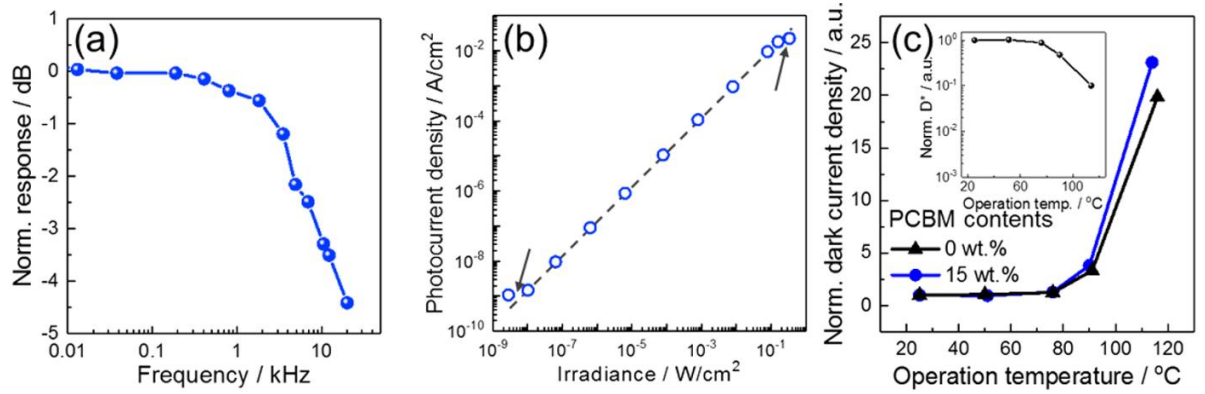


Figure 2.2.5 (a) Bode plot, (b) linear dynamic range (LDR) plot at -1 V, and (c) normalized dark current as a function of operating temperature of devices. The arrows in (b) indicate the deviation points from linearity, and the inset of (c) depicts corresponding change of specific detectivity (D^*) according to dark current.

The -3 dB frequency was measured to determine the transient response; the -3 dB frequency is the frequency corresponding to -3 dB ($\sim 70.7\%$) of the original signal. We measured the photo signal-magnitude change as a function of the frequency of the incident light and the results can be found in Figure 2.2.5(a). The measured -3 dB frequency was 9.1 kHz, which is sufficiently high for imaging applications. Theoretically, the -3 dB frequency ($f_{-3\text{dB}}$) can be calculated by Equation 2.1.5. From the transit time values in both charge carrier cases, ~ 60 μs , the calculated $f_{-3\text{dB,t}}$ value was 9.3 kHz. Since the measured -3 dB frequency is nearly same as $f_{-3\text{dB,t}}$, it can be said that the measured $f_{-3\text{dB}}$ is mainly determined by transit-time-limited -3 dB frequency.

The LDR is the range over which the responsivity stays constant and it can be calculated from the Equation 2.1.6. The measured LDR of the optimized device can be shown in Figure 2.2.5(b) and it was 142 dB, which corresponds to ~ 7 orders of magnitude. This value is superior to many inorganic-based photodetectors such as GaN (100 dB; 5 orders), InGaAs (132 dB; 6.6 orders) and comparable to Si (240 dB; 12 orders) [35]. Moreover, the slope of dashed line in Figure 5b

was 0.986 and it implies that unwanted bimolecular recombination was minimized [74]. Together with the -3 dB frequency results, it is confirmed that the optimized OPD is theoretically near ideal photodiodes.

Thermal stability at high operating temperature over ambient temperature ($25\text{ }^{\circ}\text{C}$) is considered as one of the most important factors for commercialization and industrial application of organic semiconductor-based devices. To investigate this issue, we conducted dark current measurement at high temperature ($>25\text{ }^{\circ}\text{C}$). Samples were placed on hot plate of various temperature from 50 to $115\text{ }^{\circ}\text{C}$ during dark current measurement and a sample with which PC_{61}BM is not included was also examined for comparison. The results of this investigation are summarized at Figure 5c. In both cases of PC_{61}BM contents of 0 and $15\text{ wt.}\%$, dark current was maintained nearly the same as the value at ambient condition, until the operating temperature reached to $\sim 90\text{ }^{\circ}\text{C}$ and slight difference in dark current was made at $115\text{ }^{\circ}\text{C}$. It is presumably due to the relatively large interfacial area between polymer and PC_{61}BM . Because the photocurrent was nearly unchanged by the increased measurement temperature up to $90\text{ }^{\circ}\text{C}$, the optimized OPD with the PC_{61}BM content of $15\text{ wt.}\%$ showed outstanding thermal stability even in terms of D^* , by maintaining 50% of its initial value during at least 20 min of thermal exposure to $90\text{ }^{\circ}\text{C}$ (inset of Figure 2.2.5(c)). We could conclude that the nature of Schottky junction of the optimized OPD in this work cannot only block the dark current injection under the reverse bias, but also enhance thermal stability driven by morphological simplicity.

2.2.3.2 Optical design for suppression of band II absorption

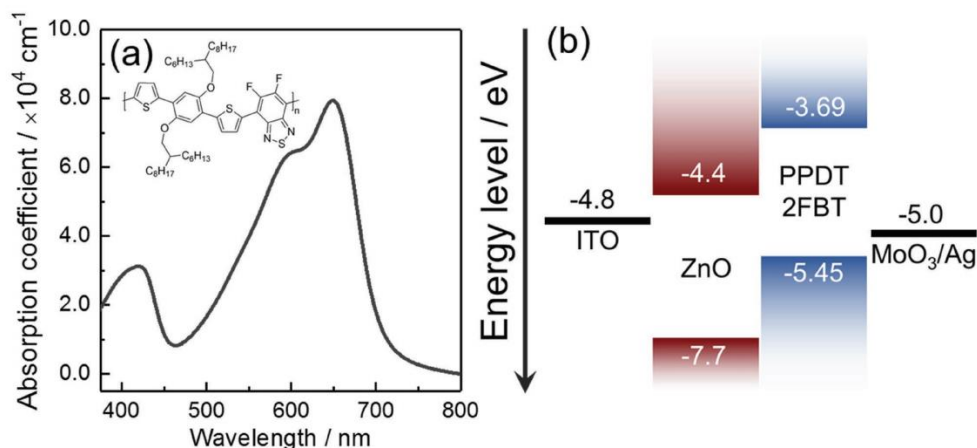


Figure 2.2.6 (a) Absorption spectrum of PPDT2FBT film and (b) energy level diagram of a Schottky junction OPD device. The inset in Figure 2.2.6(a) is the molecular structure of PPDT2FBT.

Figure 2.2.6(a) shows the chemical structure of PPDT2FBT and its UV-visible absorption spectrum in the film. Typical dual-band absorption is observed and the film absorption coefficients of the absorption peaks are 7.9×10^4 and $3.1 \times 10^4 \text{ cm}^{-1}$ for band I and band II, respectively, which correspond to the 90% absorption depth of 291 and 743 nm, respectively. This means that ~291 nm thick and ~743 nm thick PPDT2FBT films are sufficient to absorb 90% of the 650 nm and 420 nm photon fluxes, respectively. Therefore, PPDT2FBT can be an ideal photoactive material for red-selective thin film photodiodes when band II absorption can be avoided. The Schottky junction device architecture of ITO/ZnO/PPDT2FBT/MoO₃/Ag was fabricated and its energy level diagram is shown in Figure 2.2.6(b). The energy level values of ITO, ZnO, MoO₃, and Ag

were optimized with 4D beamline at the Pohang Accelerator Laboratory (PAL) in Korea. Here, a Schottky junction geometry was introduced not only to suppress unwanted dark current injection under reverse bias, but also to block blue incident photons, as discussed below.

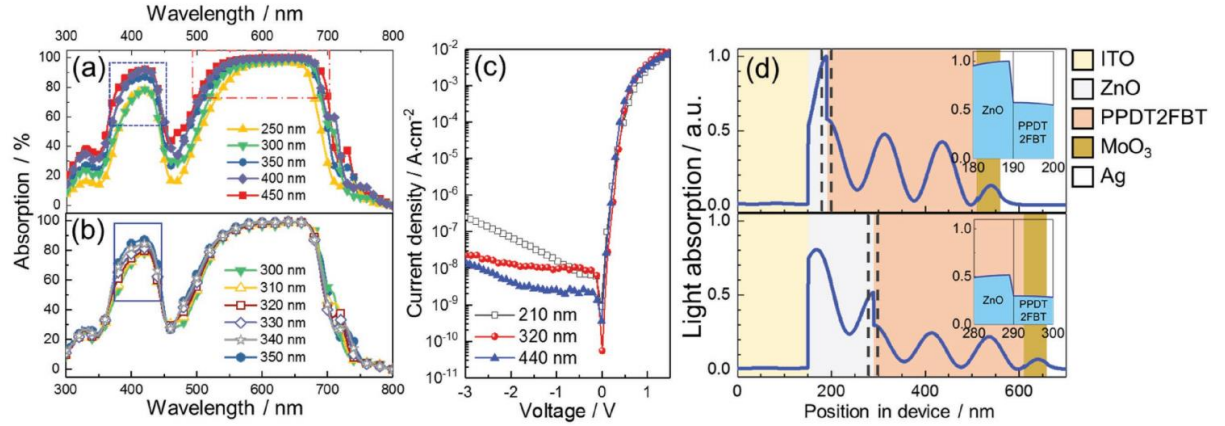


Figure 2.2.7 (a,b) Simulated results of light absorption of PPDT2FBT film by varying the active layer thickness ((a): 250–450 nm, (b): 300–350 nm), (c) measured dark J - V characteristics with various active layer thickness, and (d) the light absorption simulation results of ITO/ZnO/PPDT2FBT/MoO₃/Ag structure for deep blue ($\lambda = 400$ nm) incident photon by varying the ZnO layer thickness (upper: 40 nm, lower: 140 nm). The insets in Figure 2.2.7(d) indicate the magnified view of the black dashed box in Figure 2.2.7(d). Sky blue area denotes the amount of light absorbed within the depletion region of ZnO/PPDT2FBT junction. Thickness values of the rest of the layers are 150, 320, 50, and 150 nm for ITO, PPDT2FBT, MoO₃, and Ag, respectively

We first focused on the different absorption coefficients of band I and band II for PPDT2FBT. Because the overall absorption coefficient value is higher in band I, we can speculate that the relative absorption of band II can be further suppressed by controlling the thickness of the PPDT2FBT film from its 90% absorption depth (~ 291 nm) for photons of band I. To quantitatively obtain information on the relative absorption behaviors for band I and band II, optical

simulations were conducted using the transfer matrix method[65,66]. Experimentally obtained refractive index and extinction coefficient of PPDT2FBT were used to conduct the simulation.

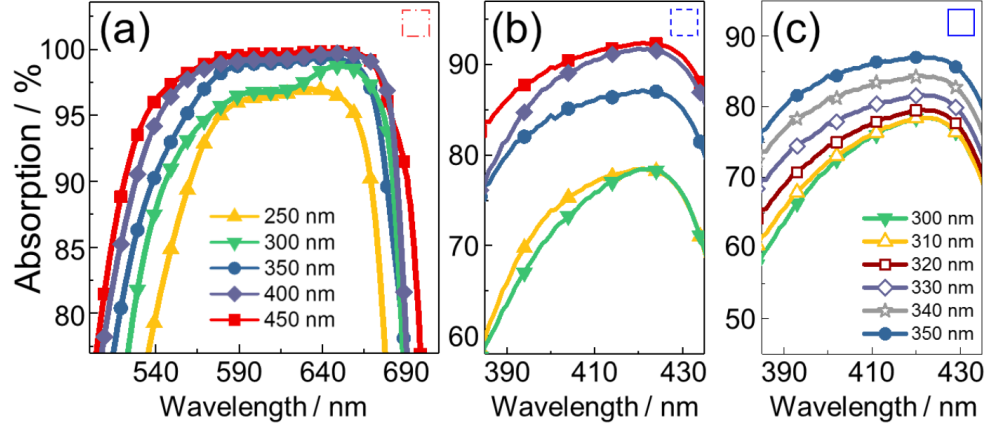


Figure 2.2.8 Magnified views of (a) red dash-dotted box, (b) blue dashed box in Figure 2.2.7(a) and (c) blue solid box in Figure 2.2.7(b).

Figure 2.2.7(a) summarizes the results with various thicknesses of PPDT2FBT films. When the thickness of PPDT2FBT decreases from 450 to 300 nm, the peak value of band I decreases by only 4%, mainly because of its high absorption coefficient (Figure 2.2.8(a)). However, for the same thickness variation, the peak value of band II significantly decreases by 18% (Figure 2.2.8(b)), which can enhance the red-selectivity of the PPDT2FBT-based OPD. The simulation results for the 300–350 nm region are shown in Figure 2.2.7(b) and Figure 2.2.8(c) to obtain more precise information in relation to the thickness. It can be shown that the band II-suppressing effect is almost saturated at a thickness of 320 nm. Since the thickness lower than 300 nm resulted in

only significant increases of dark current of the fabricated photodiode without enhancing the color-selectivity, the optimal thickness of the PPDT2FBT layer was set to 320 nm. As shown in Figure 2.2.7(c), a 440-nm thick layer enabled further suppression of the dark current, such a thick layer limited the red-selective absorption of PPDT2FBT.

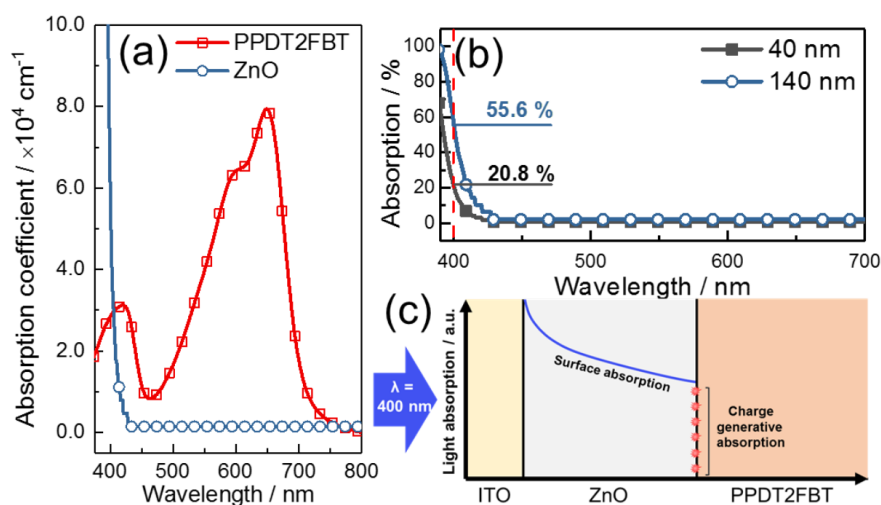


Figure 2.2.9 (a) Absorption coefficient spectra of PPDT2FBT and ZnO films, (b) the UV-Vis absorption spectra of ZnO with varying the thickness of 40 nm and 140 nm and (c) the schematic of deep blue light (400 nm) absorption in case of thick ZnO layer.

To further suppress band II absorption of PPDT2FBT, we introduced a sol-gel synthesized ZnO layer prior to the PPDT2FBT layer in the illumination pathway. PPDT2FBT and ZnO have well-aligned frontier energy levels for efficient electron and hole transfer (Figure 2.2.6(b)). Here, the introduction of ZnO has dual functions as both a deep blue-filter layer and electron-acceptor layer. First, the illuminated 400 nm photon, which corresponds to absorption band II of

PPDT2FBT, can be effectively absorbed by the ZnO layer because of its high absorption coefficient of $5.8 \times 10^4 \text{ cm}^{-1}$ (Figure 2.2.9(a)). Increasing the thickness of the ZnO layer can be beneficial for a stronger blue-filtering effect by suppressing the charge generative absorption of the blue photons at the ZnO/PPDT2FBT interface. As described in Figure 2.2.9(b), a large portion of the blue photon flux is absorbed at the ITO-headed surface and bulk of the ZnO layer, and only a small portion can be dissociated into a hole and electron when the thickness of ZnO becomes sufficiently thick (up to 140 nm). Therefore, the introduction of a ZnO layer enables full reflection of the absorption feature of band I of PPDT2FBT while suppressing band II and the excitons generated by the absorbed photons at donor/acceptor interface separate into electrons and holes by built-in potential between ZnO and PPDT2FBT and become photocurrent. More quantitative optical information can be obtained from the light absorption simulation using the transfer matrix method (Figure 2.2.7(d)). Since charge generative absorption only occurs near the ZnO/PPDT2FBT interface because of the short exciton diffusion length ($\sim 10 \text{ nm}$) of organic semiconductors, the number of generated charge carriers is proportional to the number of absorbed photons near the interface or depletion region. If we assume that the depletion width of the ZnO/PPDT2FBT Schottky junction is 20 nm with symmetric diffusion to both sides, we can

compare the relative charge generative absorption by calculating the area of depletion region (blue regions in the inset of Figure 2.2.7(d)). The relative charge generative absorption quantity for an incident 400 nm photon becomes ~52% from the increase of the ZnO layer thickness from 40 to 140 nm. Therefore, light absorption in the unwanted wavelength range could be decreased by the “optical filter” effect of the thicker ZnO layer. Although further increases in the ZnO thickness could accelerate the deep blue color filter effect, we chose 140 nm as an optimal thickness to optimize the transit time spread. The transit times calculated by considering the device geometry were found to be nearly same for hole (7.36 μ s) and electron (7.4 μ s) for 320 nm thick PPDT2FBT and 140 nm thick ZnO, respectively. Therefore, further increases in the ZnO thickness can yield significant damage on transit time spread and thus on temporal response of OPD.

Secondly, the introduction of ZnO in front of PPDT2FBT enables a Schottky junction geometry, which is beneficial for dark current suppression [64]. Concurrently, ITO/ZnO/PPDT2FBT/MoO₃/Ag with a Schottky junction between ITO/ZnO and PPDT2FBT can very efficiently block the unnecessary electron/hole injection under reverse bias, which can be beneficial for low dark currents and thus with the low shot noise of OPD [64].

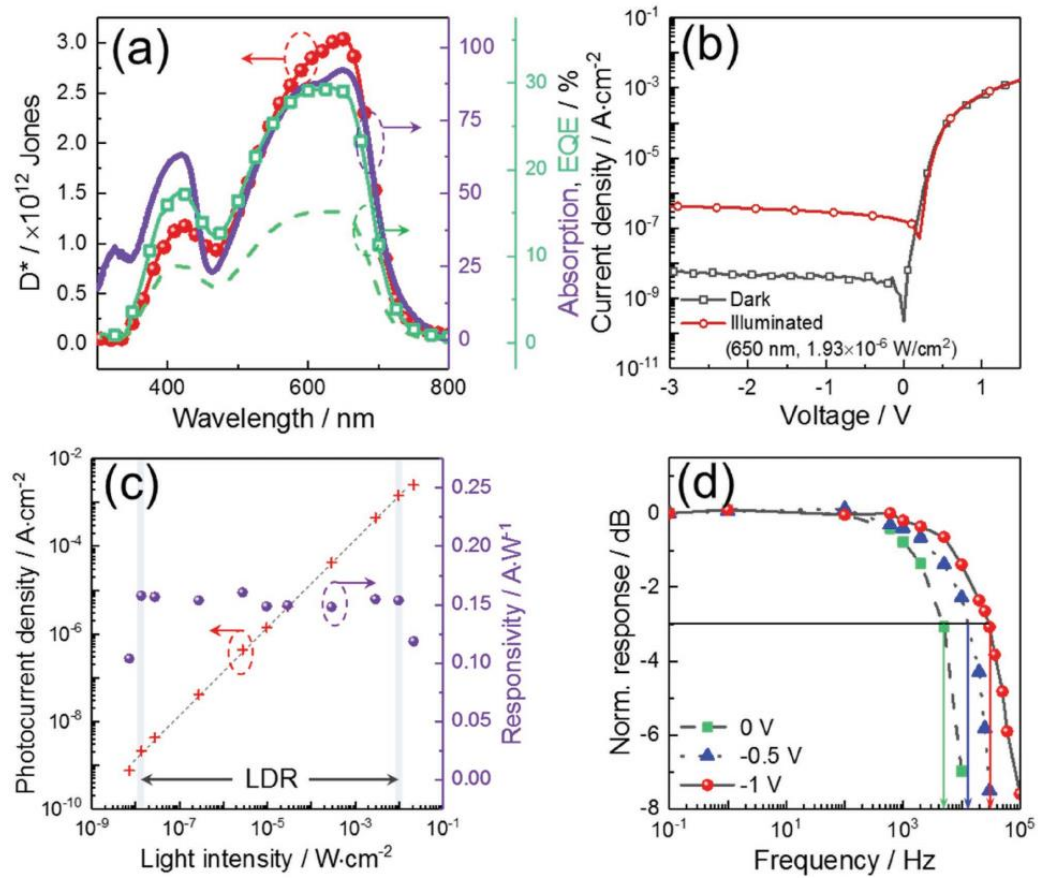


Figure 2.2.10 (a) The specific detectivity spectrum measured at -1 V (red sphere) together with the absorption spectrum of PPDT2FBT film with thickness of 320 nm (purple line) and external quantum efficiency spectrum at 0 and -1 V (green dashed line and green solid line with open square, respectively), (b) the J - V characteristics, (c) the dynamic response at -1 V together with the corresponding responsivity data, and (d) frequency responses of the optimized photodiode structure measured under various reverse biases.

Based on these synergetic contributions of ZnO together with the thickness optimization of the photoactive layer, we successfully demonstrated a high-performance red-selective thin film OPD. Band II absorption is negligibly reflected to the detectivity spectrum by optical

manipulation, while band I is fully transferred to red-selective detectivity with a peak detectivity of 3.04×10^{12} Jones (Figure 2.2.10(a)).

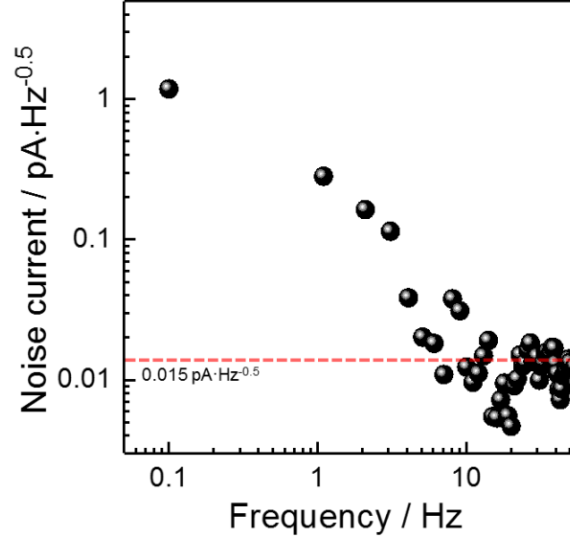


Figure 2.2.11 Noise current of the optimized photodiode at -1 V.

The specific detectivity was calculated using Equation 2.1.2. We observe a low noise current of $0.015 \text{ pA/Hz}^{0.5}$ (Figure 2.2.11) and low dark current density of $5.9 \times 10^{-9} \text{ A/cm}^2$ at -3 V (Figure 2.2.10(b)); these low dark and noise currents can be attributed to the well-defined Schottky junction structure, which can suppress unnecessary dark current injection. We address that the measured photocurrent and EQE were quite low compared to those of recently reported high performance OPDs [24,75] due to the limited carrier generation region in Schottky junction structure. However, we adapted Schottky junction structure for not only suppression of injecting dark

current, but also color filter effect for deep blue photons. Therefore, it can be said that EQE was inevitably sacrificed for high color-selectivity and low dark current.

In addition, a flat dark current density curve in the reverse saturation regime is observed. A flattened dark current density curve is caused by the suppressed tunneling current from electrodes to the active layer [28]. Thus, we can speculate that nearly ideal red-selective OPDs were realized due to the efficient charge blocking nature of them under the reverse bias.

The dynamic range is another important figure-of-merit of OPD, together with the specific detectivity. To investigate the dynamic range of the optimized red-selective OPD, we conducted LDR measurements. LDR is the photocurrent range over which the photocurrent density shows a linear relationship with respect to the light intensity [76] and can be calculated from Equation 2.1.6. The calculated LDR is 116 dB, which corresponds to nearly six orders of magnitude. This is comparable to the values of inorganic photodetectors, such as InGaAs (six orders of magnitude, 132 dB) [35] and GaN (five orders of magnitude, 100 dB) [77]. Furthermore, the slope of the fitted line in Figure 2.2.10(c) is 0.98, which is nearly unity, indicating efficient suppression of bimolecular charge recombination [74].

Temporal response measurements were performed to investigate the speed of response of the optimized OPD structure, or -3 dB bandwidth ($f_{-3\text{dB}}$). $f_{-3\text{dB}}$ is the light modulation bandwidth where the magnitude of the photo-induced signal is within -3 dB (approximately 70.7%) of the original signal (i.e., at 0 Hz). The measured $f_{-3\text{dB}}$ value is 30.6 kHz at -1 V and thus response time of the optimized OPD can be calculated as $18 \mu\text{s}$, which is sufficient for imaging applications (Figure 2.2.10(d)).

Theoretically, $f_{-3\text{dB}}$ can be calculated by Equation 2.1.5. They can be defined as

$$f_t = \frac{3.5}{2\pi t_{tr}} \quad (\text{Equation 2.2.5})$$

and

$$f_{RC} = \frac{1}{2\pi RC} \quad (\text{Equation 2.2.6})$$

, where t_{tr} is carrier transit time, R and C are the total series resistance and capacitance of the OPD, respectively [1,36]. From the measured series resistance and capacitance, f_t and f_{RC} are ~ 75 kHz and ~ 17 kHz at -1 V, respectively. We want to address that f_t of electron and hole were nearly same in the case of the optimized OPD, presumably due to the nature of Schottky junction which resulted in minimization of transit time spread. Therefore, by comparing the calculated theoretical f_t and f_{RC} , it is speculated that the measured $f_{-3\text{dB}}$ is more dependent on carrier transit

time-limited -3 dB frequency than RC-limited -3 dB frequency, which can be clearly seen in

Figure 2.2.12 below.

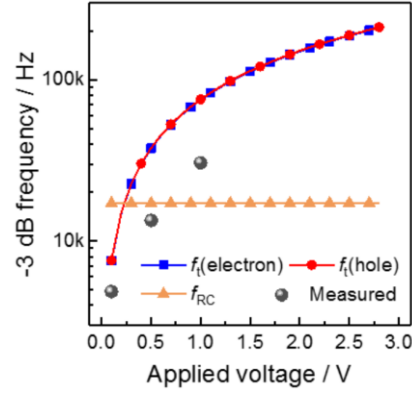


Figure 2.2.12 The measured -3 dB frequency versus applied voltage plot. For comparison, transit time-limited and RC-limited -3 dB frequency plots are included.

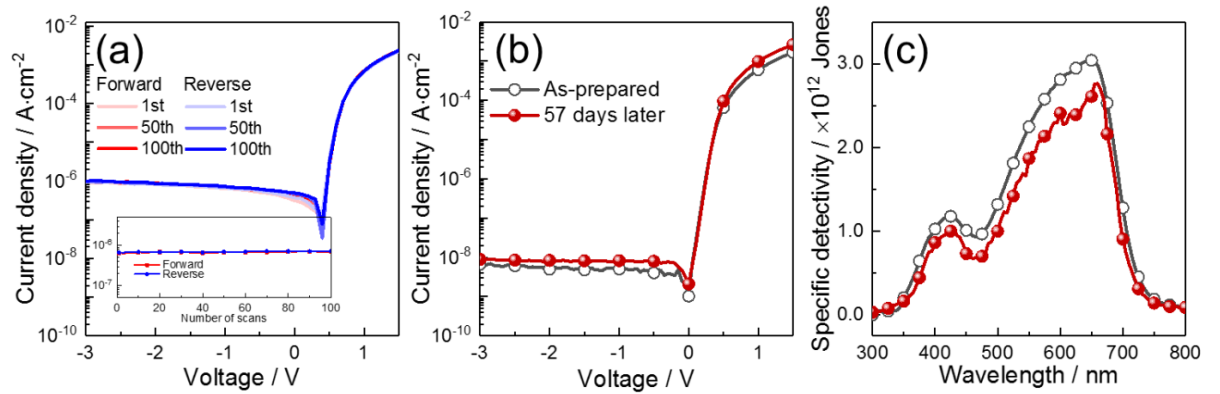


Figure 2.2.13 Performance changes (a) after 100 times of cyclically scanned J - V characteristics under 650 nm light illumination, performance changes in (b) dark current density and (c) specific detectivity of the optimized OPD measured at -1 V for 57 days of air exposure in dark condition. The inset of Figure 2.2.13(a) is the photocurrent density values at -1 V as a function of number of scans.

The operating stability of the optimized OPD was tested by continuously and cyclically scanning current density - voltage curves for 100 times. As summarized in Figure 2.2.13(a), the initial

photocurrent was well-preserved after 100 times of continuous scan thus maintaining >90% of initial photocurrent density. Additionally, the shelf-stability of the optimized OPD against air was investigated in terms of dark current density and specific detectivity. The dark current density and specific detectivity spectrum of the 57-day-old samples stored in air and dark condition were measured and compared with those of as-prepared. As can be seen in Figure 2.2.13(b) and 2.2.13(c), both dark current and specific detectivity maintained about ~90% of the initial performance. Such high stability is presumably due to highly stable electrodes (ITO/ZnO, Ag), inter-layer (MoO_3) and photoactive layer (PPDT2FBT) against air.

2.3 Etalon-electrode approach with a single photoactive layer

2.3.1 Introduction

Recently, color selective (color filter-free) thin film (thickness $< 1 \mu\text{m}$) photodiodes using organic semiconductors have been extensively studied. Research results thus far on realizing R-/G-/B-selective photodiodes can be classified into two categories: in the first one, the molecular structure of semiconductor is tuned so that the light absorbing wavelength window of the semiconductor is matched to R/G/B [9-13]; in the second one, R-/G-/B-selectivity is artificially achieved *via* selective extraction of photons with targeted wavelength [31,78]. The first method is most widely adapted for organic semiconductors due to their relative easiness of achieving wavelength selective absorption by adjusting the degree of π -conjugation. In this case, it is important to develop a diode architecture optimized to completely reflect the absorption spectrum of a semiconductor material to the final detectivity spectrum. For example, Chung *et al.* have demonstrated overall ascendancy of Schottky junction diode architecture where a single semiconductor material with narrow absorption spectrum is fully responsible for not only a well-defined R/G/B selectivity, but also for a low dark current of the resulting photodiode, over the traditional p - n junction diode [13,64,79]. As a result, thin film (active layer thickness $< 500 \text{ nm}$) and high detectivity (specific detectivity, D^* , $> 10^{12}$ Jones) R/G/B-selective OPDs with narrow

FWHM were demonstrated. The second method can be represented by charge collection narrowing (CCN) method, which utilizes different absorption behaviors between photons with high and low absorption coefficients within semiconductor active layers [31]. This enables the extraction of electrical signals only from photons with targeted wavelength. By using this method, R/G/B-selective narrowband photodiodes have been demonstrated with both organic and inorganic nanocrystals [31,78,80-86]. Although these two methods were successful on realizing R-/G-/B-selective photodiodes, the first method has a limitation in realizing narrowband red-selectivity, which can be ascribed to the dual band absorption nature of donor-acceptor type copolymers, and the second method has a distinct disadvantage in that the thickness of photoactive layer is too thick ($>1.5\ \mu\text{m}$), such that the degree-of-integration is limited. More importantly, we want to address the fact that those previous methods are not adequate for realizing micron-sized patterned pixels of image sensors, when it is considered that these methods require the use of different semiconductor materials or different thicknesses for each R/G/B pixel, both of which are not technically easy to realize. In addition, since these previous methods rely on the use of ITO electrodes, there is a definite limitation in applications to future electronic industry, which require low production cost and flexibility.

In this study, we suggest the use of an optically active, etalon-electrode where the role of color filters is embedded so that precisely patterned, color filter-free and thin film pixels of image sensors can be realized in conjunction with high performance panchromatic organic photodiodes. The suggested etalon-electrode has an optical structure consisting of Ag/optical spacer/Ag, therefore, following the principle of Fabry-Pérot interferometer, R-/G-/B-selectivity of pixels composed of etalon-electrode/panchromatic organic active layer/reflective counter electrode structure can be demonstrated by simply adjusting the thickness of optical spacer, while maintaining a small overall thickness (<800 nm). As a result, we realized a pattern of 10×10 square-shaped R/G/B image pixels with a $500\text{ }\mu\text{m}$ pitch length, all of which yielded high average detectivity values over 10^{11} Jones. Furthermore, the actual full color image capturing ability of the developed etalon-electrode-driven color filter free-image sensor was verified.

2.3.2 Experimental details

Materials Chlorobenzene, LiF were purchased from Sigma-Aldrich. P3HT, PTB7-Th and PC₇₁BM were purchased from Rieke, 1-Material and Nano-C, respectively. Purchased materials were used without further purification steps.

Photodiode fabrication To fabricate panchromatic OPD, ITO-patterned glass substrates were cleaned sequentially with detergent (Mucosal), distilled water, acetone and 2-propanol by sonication and dried with nitrogen. For etalon-electrode-based OPDs, etalon-electrodes were used instead of ITO electrode and etalon-electrodes were deposited onto the cleaned glass substrate by sequential thermal evaporation with deposition rate below 0.5 Å/s for all layers. Then 30 nm of MoO₃ hole extraction layer was deposited onto the cleaned ITO electrode or the etalon-electrodes. The semiconductor solutions with various composition ratios dissolved in chlorobenzene were spin-coated on the ITO/MoO₃ or etalon-electrodes/MoO₃ layers to have a thickness of ~390 nm. Total concentration of the solution was fixed to 35 mg/ml. For fabricating OPD array, each active layer was spatially isolated with a diamond cutter to minimize the pixel-to-pixel interference. Cathodes consisting of LiF (1 nm) and Al (100 nm) were then deposited on top of the photoactive layer by sequential thermal evaporation (rate: <0.1 Å/s for LiF and <1.0 Å/s for Al). The photoactive areas of normal and pixel device were 0.09 cm² and 0.25 mm², respectively. The fabricated OPDs were measured with lab-built jigs.

Device characterization Dark current and photocurrent measurements were performed with Keithley 2450 sourcemeter and monochromatized light from 150W Xe arc lamp controlled by Oriel Cornerstone 130 1/8 m monochromator. For measuring linear dynamic range, R/G/B lasers

(650, 520 and 445 nm, respectively) were additionally used for measuring the light intensity range above 0.1 mW/cm². Noise current was directly measured from SR830 Lock-in Amplifier. Absorbance, transmittance and reflectance for calculation of optical constants or obtaining absorbance spectra were measured from CARY5000 UV-Vis-NIR spectrometer.

Calculation of normalized photocurrent distribution The collected photocurrent values from each pixel were normalized to the maximum photocurrent of the corresponding color. For example, if four pixels have photocurrent values of 200, 40, 30 and 2 nA/cm² from red light exposure, the normalized photocurrent values from red light exposure were assumed as 1, 0.2, 0.15 and 0.01, respectively. Then the normalized photocurrent values were multiplied by 255 and rounded off to obtain the color code for each color. For example, if normalized photocurrent coordinates of one pixel is calculated as (R, G, B) = (0.9, 0.1, 0.01), the corresponding color code will be (230, 26, 3), which is nearly pure red. Therefore, if pixels have low photocurrent value because the wavelength of incident light does not match the selection wavelength of etalon-electrode or shadow mask blocks the incident light, those pixels will be displayed as near-black.

2.3.3 Results and discussion

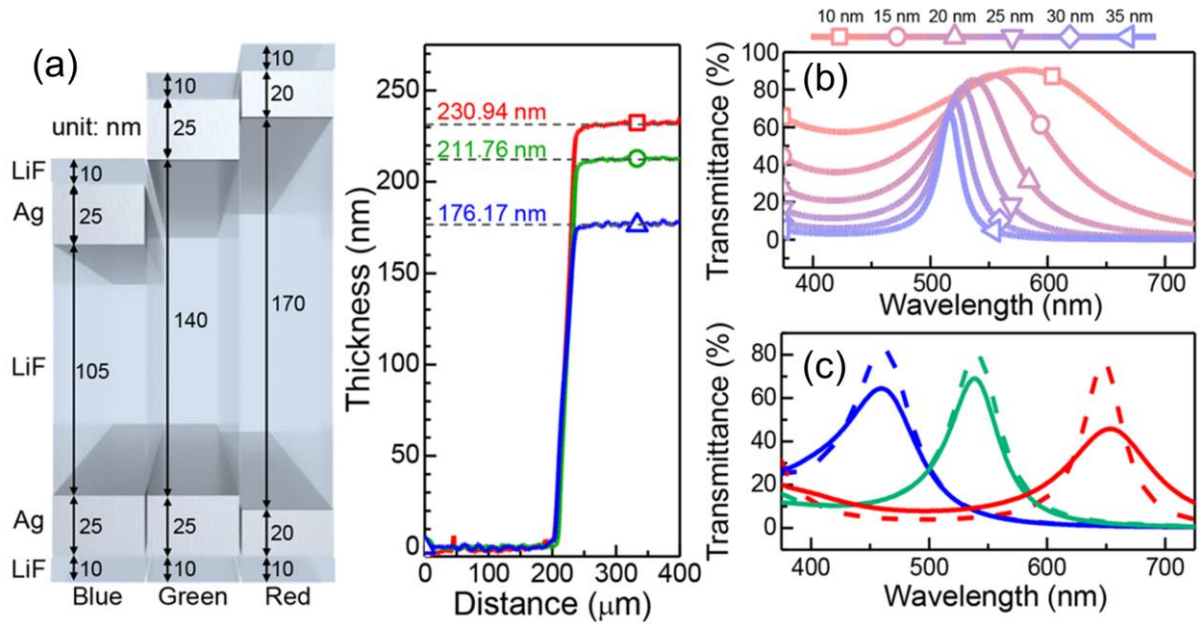


Figure 2.3.1 (a) Schematic illustration of etalon-electrode structures (left) and thickness profiles of the optimized R/G/B-selective etalon-electrodes (right), (b) simulated transmittance spectra with various Ag thicknesses, and (c) transmittance spectra with respect to central optical spacer thickness (dashed line: simulated, solid line: measured). Optical spacer thickness was fixed to 140 nm in (b), and reflective electrode thicknesses were fixed to 25 nm in (c) for simulation.

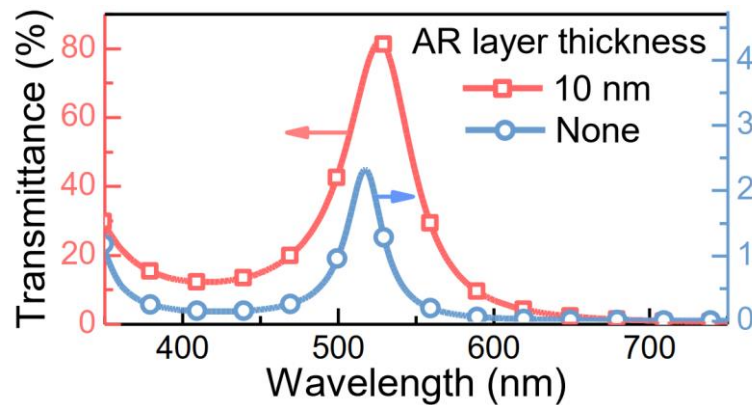


Figure 2.3.2 Simulated transmittance spectra of the Ag/LiF/Ag etalon electrodes with (red line with square) or without (blue line with circle) 10-nm-thick LiF anti-reflection layers on both external sides. Other layers except anti-reflection layers were fixed to Ag/LiF/Ag=25/135/25 nm.

A key idea of this work is embedding a color filter function into the illumination electrode, such that the organic photodiode itself can distinguish colors and extract electrical signals from the targeted wavelength without the aid of color filters. For this purpose, we adopted the concept of Fabry-Pérot etalon, where the thickness of the optical spacer determines the wavelength of the extracted optical flux. The proposed structure of the developed etalon-electrode is shown in Figure 2.3.1(a). Basically, it is a transparent optical spacer sandwiched with reflective metal: for example, only targeted wavelength can selectively penetrate the Ag/LiF/Ag structure by multiple interferences inside the interferometer. To minimize the reflection of the interferometer due to reflectance of Ag outside the interferometer, an anti-reflection (AR) layer composed of same material as optical spacer was applied on both external sides of the reflective metal layer such that the optimized etalon-electrode has a constituting structure of LiF/Ag/LiF/Ag/LiF. As seen in the simulated result in Figure 2.3.2, peak transmittance was significantly increased after 10 nm of AR layer was deposited, which was composed of the same material as the optical spacer layer, from ~2% to ~80%; this may be attributed to the decrease of refractive index difference in the air/interferometer interface. This significant change in reflectance as a result of the introduction

of AR layer can be found in various published articles [87,88]. The transmittance (T) of Fabry-Pérot interferometer can be calculated by an equation:

$$T = \frac{1}{1 + F \sin^2\left(\frac{\delta}{2}\right)} \quad (\text{Equation 2.3.1})$$

, where $F = \frac{4R}{(1-R)^2}$ is the coefficient of finesse, $\delta = \left(\frac{2\pi}{\lambda}\right) 2nl\cos\theta$ is the phase difference, R is the reflectance of metal electrode, n and l is the refractive index and thickness of optical spacer, respectively [89]. The coefficient of finesse is related to the FWHM of the transmittance spectrum, that is decreased as coefficient of finesse is increased. Therefore, the peak wavelength and the FWHM of transmittance spectrum can be tuned minutely by controlling the thickness of optical spacer and reflective metal layers. To enhance the transmittance of the interferometer, reflectance of the metal layers should be suppressed; however, reflectance needs to be partly enhanced to have sufficiently high finesse, which is related with sufficiently narrow FWHM for accurate color selection. Accordingly, we firstly optimized the thicknesses of reflective metal layers, while the other thickness values were set constant. Optical simulation was conducted by the transfer matrix method. We simulated various thickness values of reflective metal layers, from 10 to 35 nm for each layer, and the simulation results can be seen in Figure 2.3.1(b). It is clearly seen that peak transmittance was significantly decreased from ~90% to ~67%, which is due to

the decrease of transmittance by the increase of Ag thicknesses. Simultaneously, as Ag thickness increased, FWHM was narrowed, which can be ascribed to the increased coefficient of finesse as Ag thickness was increased.

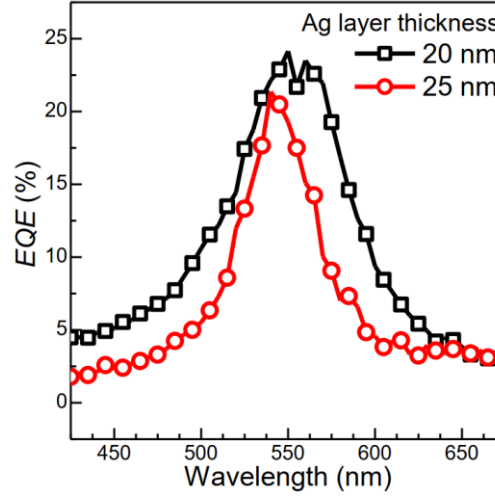


Figure 2.3.3 EQE spectra of the fabricated OPDs with green-selective etalon-electrodes with different Ag layer thickness (LiF/Ag/LiF/Ag/LiF=10/20 or 25/140/20 or 25/10 nm).

The effect of increasing Ag thickness on OPD performance was also tested and the results are summarized in Figure 2.3.3, showing that decreased light intensity given by increased Ag thickness yielded suppressed EQE. Considering the FWHM of commercially available color filters (80~120 nm), we set the optimal Ag thickness to 20 ~ 25 nm, so that the transmittance spectrum of etalon-electrode has FWHM of ~100 nm, which is preferred for image sensor applications [90,91]. Based on the information of the optimized Fabry-Pérot interferometer structure, we obtained the optimal conditions of R/G/B-selective etalon-electrode from optical simulation, which

is displayed in Figure 2.3.1(c) as dashed lines. The overall thicknesses of the optimized etalon-electrodes range from 175 nm to 230 nm, which are comparable to the thickness of conventional ITO (~150 nm). The experimental transmittance spectra for R/G/B-selective etalon-electrode closely followed the theoretically expected traces, summarized in Figure 2.3.1(c) as solid lines. The etalon-electrodes were fabricated by sequential thermal evaporation of LiF and Ag on cleaned glass substrate (evaporation rate: $<0.5 \text{ \AA/s}$ for all constituting layers), and the optimum thicknesses of each layer were LiF/Ag/LiF/Ag/LiF=10/25/105/25/10, 10/25/140/25/10 and 10/20/170/20/10 nm for blue-, green- and red-selective etalon-electrodes, respectively. As seen in this figure, the measured spectra have quite accurate peak locations with a well-defined narrowband character. Therefore, by using R-/G-/B-selective etalon-electrodes with various optical spacer thicknesses as window electrodes, we expected that the wavelength distribution of incident photons can be easily controlled and this can lead to facile control of spectral response of the resultant OPDs.

As a next step, we must develop a broadband photodiode with panchromatic spectral response over whole the visible light range, such that color selectivity can be solely dependent upon the wavelength distribution of the incident photons through etalon-electrode, while maintaining a

thin film thickness. Because inorganic semiconductor-based broadband photodiodes suffer from thick active layer thicknesses, which raises the issues of inter-pixel cross talk [1], we introduced organic photodiodes with high absorption coefficient. To fully optically absorb and electrically convert visible light, bulk heterojunction (BHJ) is mostly preferred in organic photodiodes to overcome strong exciton binding energy (>0.3 eV) of organic semiconductors. In this case, polymer-based BHJ has shown the highest EQE among all other combinations of organic semiconductors and thus, here we utilized polymer BHJ structure, but with ternary components, in constructing a solution processed BHJ to implement panchromatic absorption behavior.

In a previous report, it was demonstrated that binary BHJ consisting of low bandgap polymer and PC₇₁BM with thick film thickness over 700 nm could achieve broadband spectral response [36]. However, to fully utilize the genuine benefits of high absorption coefficient of organic semiconductor, and considering industrial demand for the CMOS image sensor, as well as the small pixel sizes (<1 μm) of commercially available unit pixels, we needed to introduce ternary heterojunction to realize complementary absorption while maintaining a film thickness of approximately 400 nm. For this purpose, we picked up P3HT:PTB7-Th and PC₇₁BM as a donor complex and acceptor, respectively.

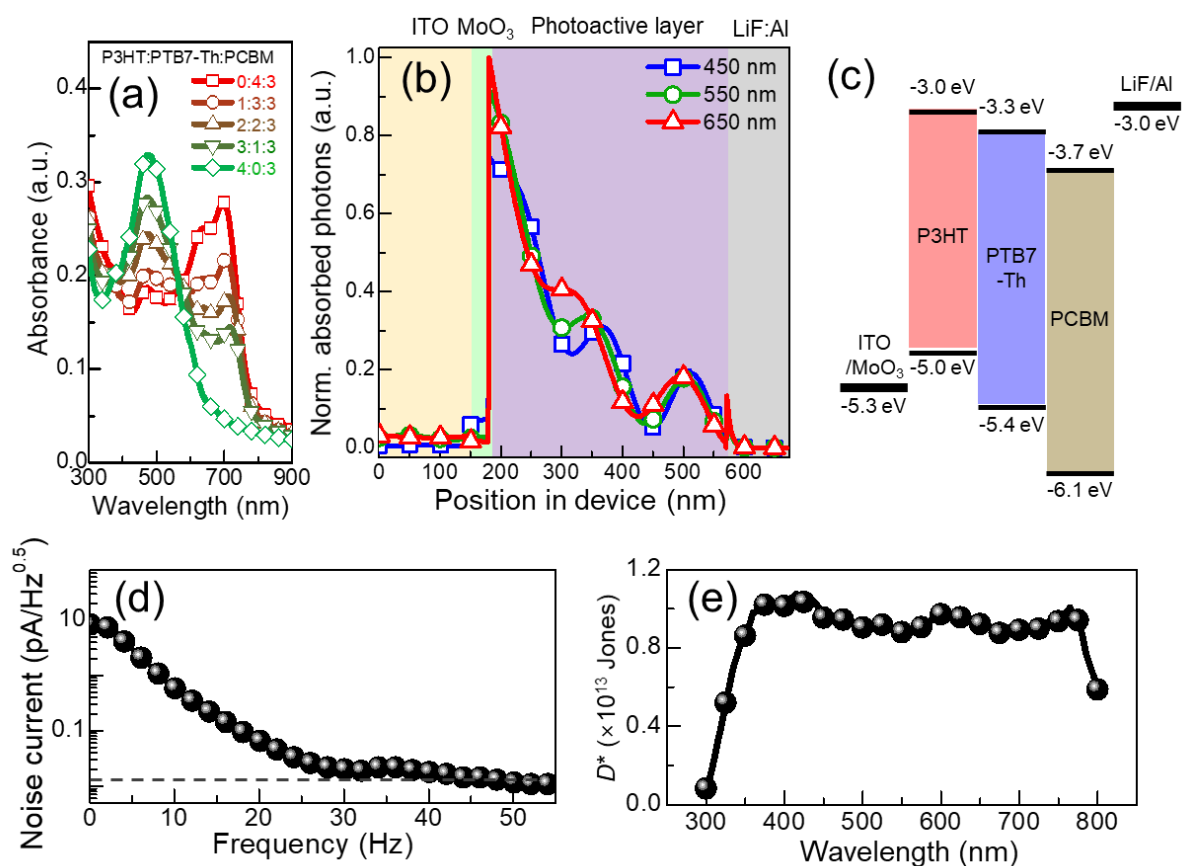


Figure 2.3.4 (a) UV–vis absorption spectra of various ternary blend combinations consisting of P3HT, PTB7-Th, and PCBM, (b) simulated normalized amount of absorbed photons in each constituting layer in OPD structure, (c) energy level diagram of used materials to fabricate OPD, (d) noise current and (e) noise current-based spectral response of the optimized panchromatic OPD at -1 V.

In Figure 2.3.4(a), the absorption spectra of pristine thin films of P3HT, PTB7-Th and PC₇₁BM are introduced together with spectra of thin films consisting of their ternary BHJ with various mixing ratios. As clearly demonstrated, an 1:3:3 mixing ratio of P3HT:PTB7-Th:PC₇₁BM can render most flattened absorption spectrum throughout whole the visible range from 400 nm to

770 nm. To observe the change in spectral response as a result of changing constituting ratio of photoactive layer, we fabricated panchromatic OPDs with various combinations of ratio for photoactive layer. Other conditions such as used materials and thicknesses of constituting layers were fixed to ITO/MoO₃ (30 nm)/Photoactive layer (~400 nm)/LiF:Al (1 nm:100 nm). As clearly seen in Figure 2.3.5 below, the resultant OPD with optimum constituting ratio for photoactive layer had not only highest average specific detectivity, but also most flattened shape of spectral response in visible range (400 – 700 nm).

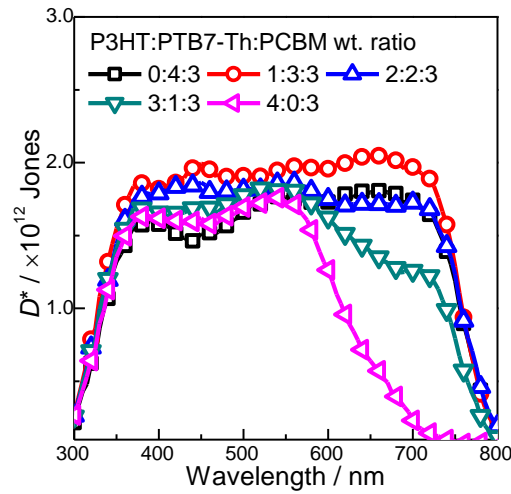


Figure 2.3.5 Dark current-based specific detectivity spectra with various composition ratios of photoactive layers under the reverse bias of 1 V. Other conditions were fixed to ITO/MoO₃(30 nm)/Photoactive layers(~400 nm)/LiF(1 nm)/Al(100 nm). For the calculation of dark current-based specific detectivity, shot noise-limited specific detectivity equation was used: $D^* = \mathfrak{R} / (2qJ_d)^{0.5}$, where \mathfrak{R} is the responsivity, q is the elementary charge and J_d is the dark current density

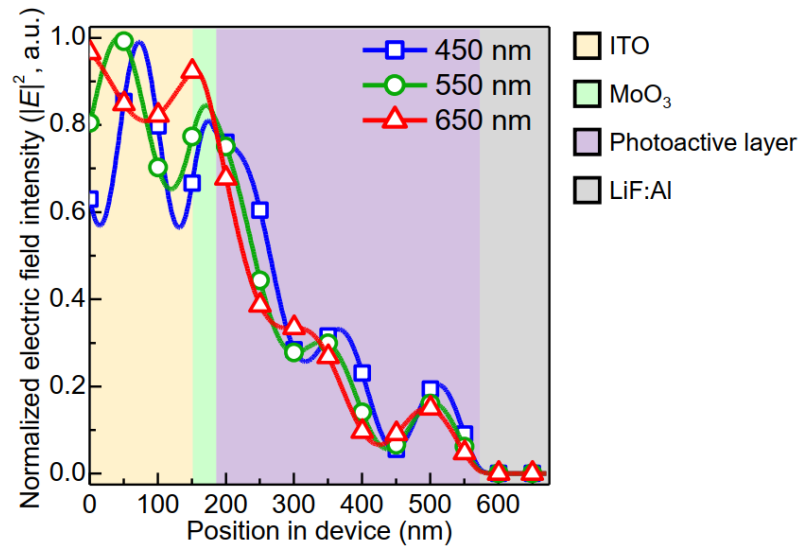


Figure 2.3.6 Simulated normalized electric field intensity of each constituting layer in OPD structure.

To further quantitatively analyze the optical phenomena in the ternary BHJ, the generalized transfer matrix method was employed [66]. Based on the experimentally obtained n and extinction coefficient (k) values of BHJ, normalized absorbed photon profiles and normalized electric field intensity ($|E|^2$) distributions were calculated within a photodiode of ITO/MoO₃/BHJ/LiF:Al structure (Figure 2.3.4(b) and Figure 2.3.6, respectively) with the thicknesses of 150/30/~390/1/100 nm, respectively. It is evident that the all visible photons with wavelengths of 450, 550 and 650 nm for representing blue, green and red photons, respectively, display Beer–Lambert type absorption behavior with negligible difference with each other, implying that panchromatic absorption feature is well preserved within ternary BHJ. Based on this, a photodiode

was fabricated with the structure of ITO/MoO₃/BHJ/LiF:Al. The energy level diagram of the diode is shown in Figure 2.3.4(c). For both HOMO and LUMO levels, P3HT/PTB7-Th/PC₇₁BM forms well-defined cascade junction structures, which are very important for efficient exciton separation and extraction. For ITO/MoO₃ and LiF/Al electrodes, we adopted previously reported work function values [92,93]. The figure-of-merit of photodiode is a specific detectivity (D^*), which can be defined as Equation 2.1.2. EQE can be calculated by

$$EQE = \frac{hcJ_{ph}}{q\lambda P} \quad (\text{Equation 2.3.2})$$

, where J_{ph} is the photocurrent density in A/cm² and P is the incident light intensity in W/cm².

To complete D^* calculation, the noise current was also measured by a lock-in amplifier and the resulting spectrum is summarized in Figure 2.3.4(d). Although a relatively small (390 nm) active layer thickness was introduced, low noise current of 0.012 pA/Hz^{0.5} at 35 Hz was obtained, which can be interpreted as low noise-equivalent power of 0.031 pW/Hz^{0.5} at 600 nm. Typically, the dark current density of an ideal diode is defined as

$$J_d = J_s \left[\exp \left(\frac{q(V - J_d R_s)}{\eta k_B T} \right) - 1 \right] \quad (\text{Equation 2.3.3})$$

, where J_s is the dark saturation current density, V is the applied voltage, R_s is the series resistance, k_B is the Boltzmann constant, T is the temperature, and η is the ideality factor [94].

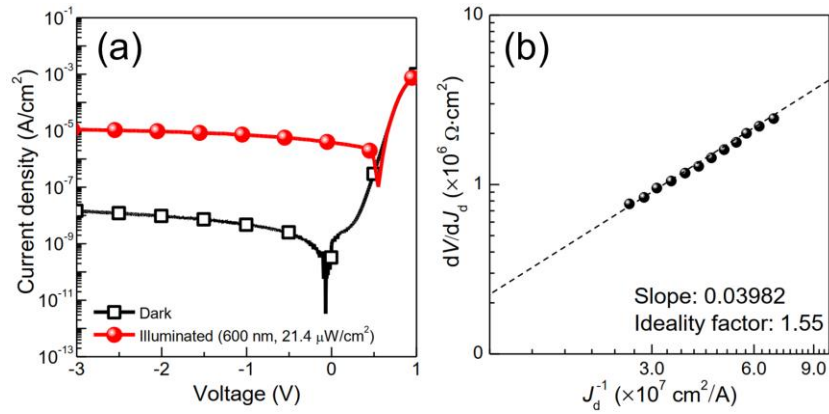


Figure 2.3.7 (a) J - V Characteristics and (b) dV/dJ_d vs J_d^{-1} plot of the optimized panchromatic OPD for calculating ideality factor.

Therefore, by replotting the measured dark J - V curve (Figure 2.3.7(a)) as dV/dJ_d vs J_d^{-1} relationship according to the Equation 2.3.3 as summarized in Figure 2.3.7(b), the ideality factor can be obtained as low as 1.55, implying that the fabricated BHJ diode is fairly free from interface trapping or bimolecular recombination [34]. By using Equation 2.1.2, D^* spectrum can be obtained, as shown in Figure 2.3.4(e). Because the used active layer thickness is only 390 nm, comparable to the penetration depth of the active layer, no other optical manipulation effects were observed, and panchromatic, broadband D^* spectrum was obtained. Reflecting ideal ternary heterojunction, high D^* near 1.0×10^{13} Jones were observed throughout whole the visible range.

The transparent electrode (ITO) of the panchromatic OPD structure was then substituted with the optimized etalon-electrode for wavelength selective, color filter free OPD fabrication. Figure

2.3.8(a) shows schematic device structure of the optimized R-/G-/B-selective OPDs and cross-section scanning electron microscope (SEM) image of the actual green-selective OPD.

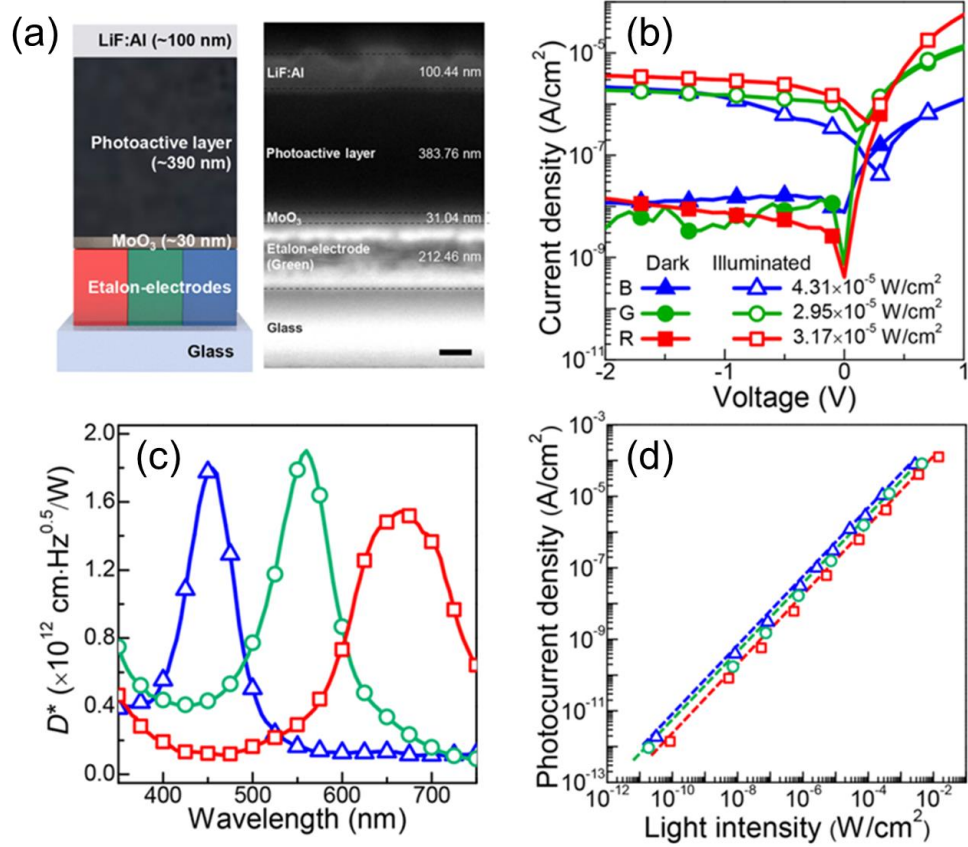


Figure 2.3.8 (a) Schematic illustration of etalon-electrode-based OPD (left) and cross-section scanning electron microscope (SEM) image of the optimized green-selective OPD (right), (b) J - V characteristics, (c) noise current-based spectral responses, and (d) LDRs of the optimized R/G/B-selective OPDs. In Figure 2.3.8(c) and 2.3.8(d), the data were measured at -1 V. The scale bar of the SEM image in (a) is 100 nm.

Despite the rather complicated structure of etalon-electrode, it can be confirmed that the total thickness of the photodiode is still far less than 1 μm due to the small thickness of the photoactive layer (390 nm), as well as the exclusion of thick ITO electrode. The total thickness values in the

order of R-, G-, and B-selective OPDs are only ~750, ~730, ~700 nm, respectively. As can be seen in Figure 2.3.8(b), measured dark J - V curves show typical diode characteristics, such as high rectification ratios and low ideality factors as summarized in Figure 2.3.9(a), comparable to that of the panchromatic OPD.

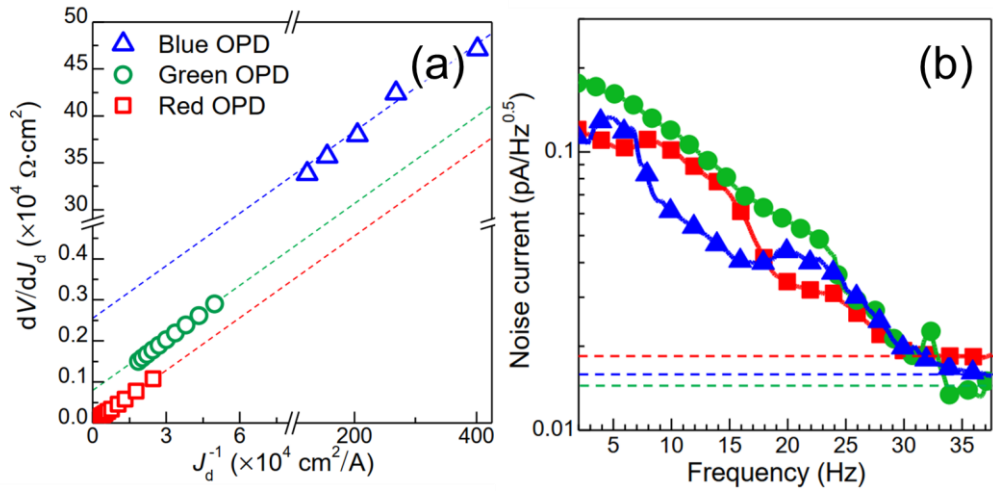


Figure 2.3.9 (a) dV/dJ_d vs J_d^{-1} plots of the optimized R/G/B-selective OPDs for calculating ideality factors, and (b) the noise current plots of the optimized R/G/B-selective OPDs. In Figure 2.3.9(a), the measured slope and ideality factor values were (slope, ideality factor) = (0.04348, 1.69), (0.04243, 1.65) and (0.04485, 1.74) for R-, G- and B-selective OPDs, respectively. In Figure 2.3.9(b), the measured noise current values of R-/G-/B-selective OPDs were 0.018, 0.014 and 0.015 pA/Hz^{0.5}, respectively.

This means that the etalon-electrode performs its own electrode function adequately at the ITO level, despite the addition of an additional function of wavelength selectivity. Nonetheless,

photocurrents were slightly decreased due to photon loss by the relatively lower transmittance of the etalon-electrode (<70%).

We measured spectral response of R-/G-/B-selective OPD by using noise current of each OPD (Figure 2.3.9(b)). As can be seen in Figure 2.3.8(c), the resultant R/G/B-selective OPDs show high peak detectivity over 1.0×10^{12} Jones at the peak wavelengths in the transmittance spectra of each corresponding etalon-electrode. Although peak values of specific detectivity spectra were quite low compared to the panchromatic devices, presumably due to the absence of perfect transmission (peak transmittance <70%), the peak detectivity values still exceeded 1.0×10^{12} Jones for all color regimes, which can be attributed to the initially very high detectivity of the panchromatic OPDs ($\sim 1.0 \times 10^{13}$ Jones). We measured photocurrent values with respect to various light intensity values to calculate LDR for R/G/B detection. (Figure 2.3.8(d)) The LDR can be defined as a photocurrent ratio or incident light intensity ratio between minimum and maximum detectable photocurrent or incident light intensity which indicates the responsivity maintains constant. In the form of an equation, LDR can be expressed as Equation 2.1.6. Actually, we could not measure the lower limit of photocurrent adequately, due to our resolution of instrument ($\sim 10^{-12}$ A); therefore, noise equivalent power (NEP) values of R/G/B-selective OPDs were calculated to elicit

inferred LDR values, since photocurrent value with respect to NEP of fabricated OPDs can be regarded as lower limit of LDR [95]. NEP can be calculated by an equation:

$$\text{NEP} = i_n/R. \quad (\text{Equation 2.3.4})$$

The measured LDR values of R-/G-/B-selective OPDs were 128, 115 and 110 dB, and the inferred LDR values were 159, 158 and 152 dB, respectively, which are comparable with those of recently reported high-performance OPDs [75,96,97].

Selection wavelength region	Active layer thickness	Dark current density	EQE	D^*	FWHM or Wavelength range	Reference
	nm	nA/cm ² (Bias V)	% (Bias V, Wavelength nm)	$\times 10^{12}$ Jones (Bias V, Wavelength nm)	nm	
Red (600~700 nm)	~2500	~600(-1)	49(-1)	0.13 (-1)	<30	[84]
	1500	~0.1(-1)	34(-1)	1.8 (-1)	<90	[31]
	390	7.63(-1)	18.0(-1)	1.55 (-1)	~120	This work
Green (500~600 nm)	90	40.1(-5)	~60.1(-5)	2.34 (-5)	131	[98]
	35	~900(-1)	15(-1)	~0.3 (-1)	80	[49]
	390	3.8(-1)	19.6(-1)	1.89 (-1)	78	This work
Blue (400~500 nm)	130	3.0(0)	22.5(-2)	-	~100	[99]
	~450	1.3(-5)	~4.5(-5)	1.15 (-5)	110	[58]
	390	14.6(-1)	24.6(-1)	1.8 (-1)	63	This work
Panchromatic (400~700 nm)	500	9(-1)	~30(-1)	1.0 (-1)	350-650	[20]
	700	~8(-1)	~70(-1)	~2.5 (-1)	330-700	[36]
	390	4.87(-1)	65.1(-1)	10.1 (-1)	400-770	This work

Table 2.3.1 Comparison of the suggested OPD with recently reported OPDs.

We compared the performance of the fabricated OPDs with those of recently reported various color selective and panchromatic OPDs in terms of photoactive layer thickness, dark current, EQE, specific detectivity and FWHM. As summarized in Table 2.3.1 above, the suggested dual

function etalon-electrode enables to achieve OPDs with high precision R/G/B color selectivity and thin active layer thickness as well as high D^* over 1.0×10^{12} Jones simultaneously, which was not possible by other methods.

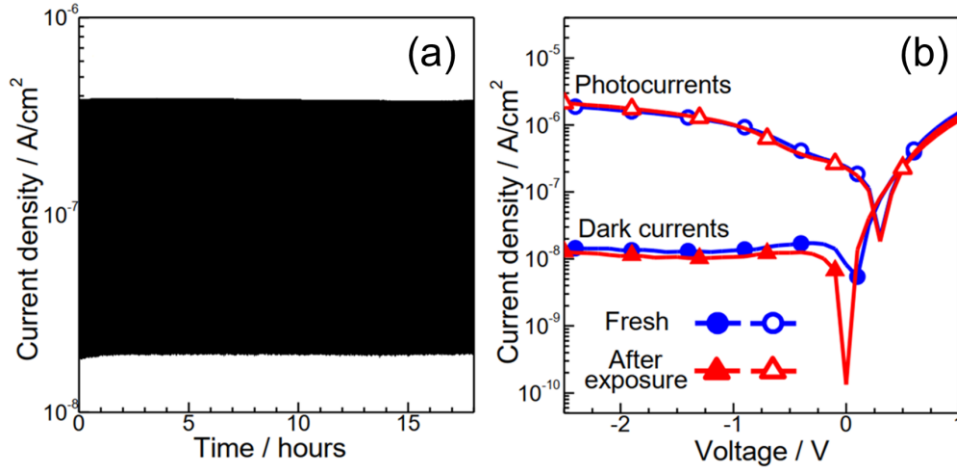


Figure 2.3.10 (a) Current-time characteristics of blue-selective OPD exposure to pulsed laser light for 18 hours, (b) J - V characteristics of the OPD before and after exposing to stability test. For Figure 2.3.10(b), a light source with the wavelength of 450 nm and the light intensity of $15.4 \mu\text{W}/\text{cm}^2$ was used.

To examine the stability of the fabricated OPD against incident light, we conducted operational stability test by using blue-selective OPD with pulsed laser (1 Hz, wavelength: 445 nm, light intensity: $5.78 \text{ mW}/\text{cm}^2$, used with 0.1% neutral density filter). As clearly seen in Figure 2.3.10(a), photocurrent and dark current were maintained nearly constant after 18 hours of light exposure. J - V characteristics of the OPD before and after exposing to stability test shown in Figure 2.3.10(b) exhibited only slight changes in both current plots.

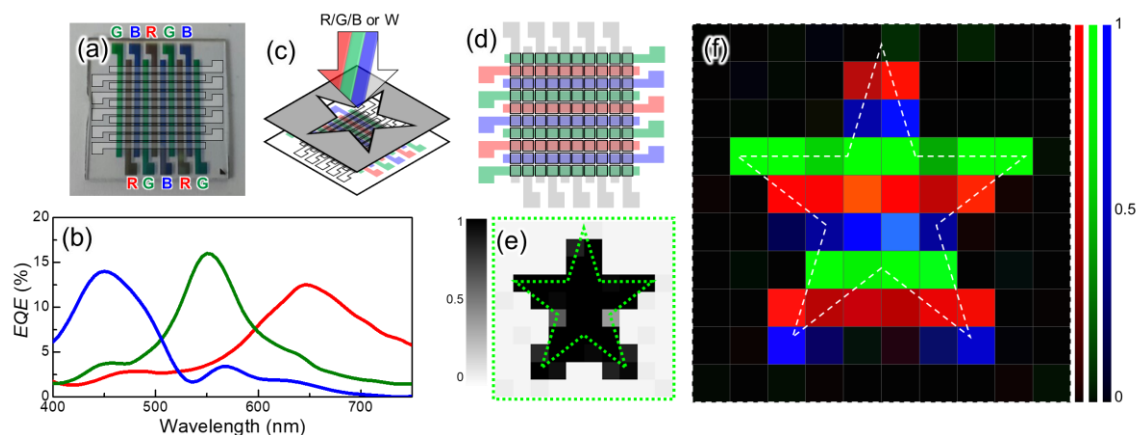


Figure 2.3.11 (a) Digital camera image of the fabricated 10 columns of etalon-electrodes, (b) measured EQE spectra of R/G/B-selective OPD pixels at -1 V, (c) a schematic illustration describing how to obtain star-shaped RGB image from R/G/B-selective OPD array, (d) configuration of OPD array which the R/G/B-pixels (black squares) were formed by sandwiching bottom R/G/B-selective etalons (pastel red, green and blue) and top reflective electrode (LiF:Al, gray), (e) normalized photocurrent distribution when white light was illuminated on the OPD array through a star-shaped shadow mask, and (f) collected result of normalized photocurrent distributions when red (650 nm, $31.7 \mu\text{W}/\text{cm}^2$), green (550 nm, $29.5 \mu\text{W}/\text{cm}^2$), and blue (450 nm, $43.1 \mu\text{W}/\text{cm}^2$) lights were illuminated on the OPD array covered with a star-shaped shadow mask. In Figure 2.3.11(a,e,f), semitransparent horizontal electrode structures and green and white dotted stars were added for the reader's convenience.

To investigate the feasibility of image sensor application, we fabricated an array of small-sized OPDs ($500 \mu\text{m} \times 500 \mu\text{m}$), with 10×10 pixels per substrate. R-, G- and B-selective etalon-electrodes with contact pads were deposited on a cleaned glass substrate as anodes by sequential thermal evaporation of LiF and Ag. As can be seen in Figure 2.3.11(a), each electrode was successfully deposited onto glass substrate with contact pads for electrical measurement.

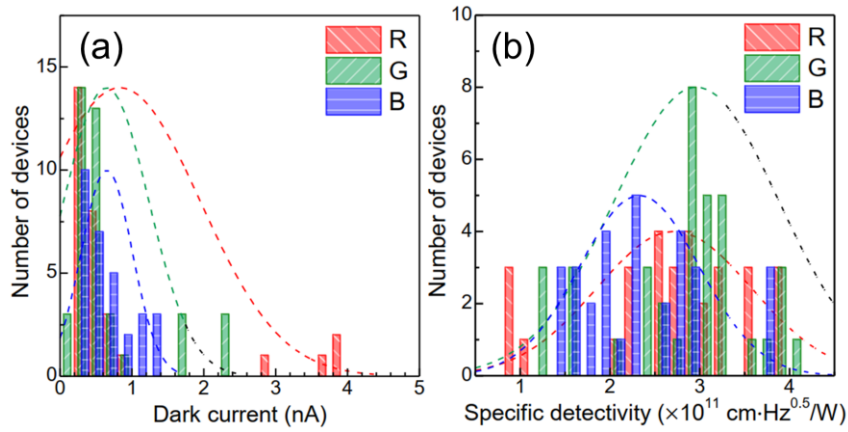


Figure 2.3.12 (a) Dark current and (b) dark current-based peak detectivity distributions of the 100 independent R/G/B-selective OPD pixels. The statistical average dark current values were 0.832 ± 1.10 nA, 0.644 ± 0.586 nA, 0.650 ± 0.348 nA and peak detectivity values were $2.714 \pm 0.848 \times 10^{11}$ Jones, $2.963 \pm 0.905 \times 10^{11}$ Jones and $2.327 \pm 0.655 \times 10^{11}$ Jones for R-, G- and B-selective OPD pixels, respectively.

As can be seen in Figure 2.3.12, uniform dark current distribution could be observed, which implies that the fabricated arrayed OPDs have high reproducibility. Figure 2.3.11(b) shows the EQE spectra of R/G/B-selective etalon-electrode at -1 V. Although FWHMs of the measured R/G/B-selective pixel OPDs were partly increased, they still maintained sufficient FWHMs of ~95 nm for B/G-selective OPDs and ~120 nm for R-selective OPD, which are narrow enough for image sensor application.

To simply verify the feasibility of the fabricated color filter-free image sensor consisting of 10×10 OPD array, we investigated image capturing capability with different light sources as well

as star-shaped shadow mask (Figure 2.3.11(c)). As can be seen in Figure 2.3.11(d), R-selective OPD pixels were located at row 2, 5 and 8, G-selective OPD pixels were located at row 1, 4, 7 and 10 and B-selective OPD pixels were located at row 3, 6 and 9. After collecting photocurrent information from 100 pixels using home-built jig and software, we reconstructed 30 levels of R/G/B color intensity according to the magnitude of the photocurrent. To test image-converting ability, four different light sources were used, white, red (650 nm), green (550 nm) and blue (450 nm). As clearly shown in Figure 2.3.11(e), we could capture a star-shaped image when white light was illuminated, because of the well-defined and uniform light-to-electricity conversion ability of all the pixels. Next, to test a color reading ability of the developed color filter-free image sensor array, R/G/B light sources of similar intensities were successively used through the star-shaped mask, and then the extracted R/G/B pixel signals were superimposed to reproduce the color image. Details of the method to obtain full color image can be found from the Method part at the end of this article.

As seen in Figure 2.3.11(f), a full color star-shape image with distinct colors could be obtained from the line consisting of each R/G/B pixel. Furthermore, in order to examine the possibility of detection of colors other than the three primary colors of R/G/B, an attempt was made to detect

the light sources having wavelengths of 400 nm, 500 nm, 600 and 700 nm as summarized in Figure 2.3.13 below.

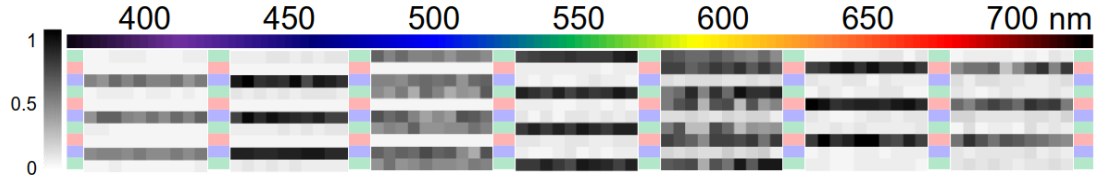


Figure 2.3.13 Normalized photocurrent distributions when the 10×10 OPD array was illuminated with various wavelengths of incident light.

Since these wavelengths are located in between the center wavelength of each R/G/B photodiode, when the light sources of 500 nm and 600 nm are used, the B, G pixels and the G, R pixels rendered their corresponding colors but with ordinary intensity, implying that various colors can be detected. If additional pixel-by-pixel separation technologies, such as using blocking diodes or banks [100,101], can be applied, we can capture much higher quality images, in which unwanted signals are nearly fully suppressed.

3 Conclusion

In conclusion, three different approaches for realizing high-performance organic semiconductor-based color filter-free photodiodes were suggested. As a result of the introduction of polyelectrolytes as interlayer, work function of the transparent electrode was efficiently shifted toward preferred direction, and the shifted WF had led to the increase of photocurrent and suppression of dark current simultaneously. Furthermore, the introduction of polyelectrolytes also led to the elimination of the interfacial defects, so that more ideal OPD with flatter dark J - V curves could be realized. By utilizing Schottky junction with color-selective donors, color-selectivity could be smoothly realized without using color filters. To enhance the spectral responses of the resultant OPDs, two different methods were used; the introduction of small amount of acceptor and the optical design for suppression of band II absorption. By introducing optimal amount of PC₆₁BM acceptor to color-selective donor layer, EQE was enhanced with negligibly increased dark current and thermal stability. As a result of the optical design for red-selective OPD, unwanted band II absorption could be effectively minimized. Lastly, a device architecture of organic photodiode is suggested for realizing color filter free, high resolution image sensors. A key structural evolution is embedding color filter function to the electrode, which is enabled by substituting conventional ITO with Fabry-Pérot etalon-electrodes. By utilizing R/G/B-selective etalon-electrodes with panchromatic absorbing photoactive layer, narrowband color selective detectivity over 10^{12} Jones with a small overall thickness (<800 nm) could be achieved. Furthermore, we also had verified the image capturing ability against incident light signal with specific shape

and incident light with various colors, using an image sensor array composed of 10×10 pixels based on a color selective photodiode with $500 \mu\text{m}$ pitch size.

4 References

- [1] Jansen-van Vuuren, R. D., Armin, A., Pandey, A. K., Burn, P. L., and Meredith, P. “Organic Photodiodes: The Future of Full Color Detection and Image Sensing.” *Adv. Mater.*, 28, 2016, pp. 4766-4802.
- [2] Saga, T. “Advances in Crystalline Silicon Solar Cell Technology for Industrial Mass Production.” *NPG Asia Mater.*, 2, 2010, pp. 96-102.
- [3] Seo, H., Aihara, S., Namba, M., Watabe, T., Ohtake, H., Kubota, M., Egami, N., Hiramatsu, T., Matsuda, T., Furuta, M., Nitta, H., and Hirao, T. “Stacked Color Image Sensor using Wavelength-Selective Organic Photoconductive Films with Zinc-Oxide Thin Film Transistors as a Signal Readout Circuit.” *Proc. SPIE*, 7536, 2010, pp. 753602.
- [4] Kim, Y., and Bradley, D. D. C. “Bright Red Emission from Single Layer Polymer Light-Emitting Devices based on Blends of Regioregular P3HT and F8BT.” *Curr. Appl. Phys.*, 5, 2005, pp. 222-226.
- [5] Che, X., Li, Y., Qu, Y., and Forrest, S. R. “High Fabrication Yield Organic Tandem Photovoltaics Combining Vacuum- and Solution Processed Subcells with 15% Efficiency.” *Nat. Energy*, 3, 2018, pp. 422-427.
- [6] Xiao, P., Mao, J., Ding, K., Luo, W., Hu, W., Zhang, X., Zhang, X., and Jie, J. “Solution-Processed 3D RGO-MoS₂/Pyramid Si Heterojunction for Ultrahigh Detectivity and Ultra-Broadband Photodetection.” *Adv. Mater.*, 30, 2018, pp. 1801729.

- [7] Deng, W., Zhang, X., Huang, L., Xu, X., Wang, L., Wang, J., Shang, Q., Lee, S. - T., and Jie, J. "Aligned Single-Crystalline Perovskite Microwire Arrays for High-Performance Flexible Image Sensors with Long-Term Stability." *Adv. Mater.*, 28, 2016, pp. 2201-2208.
- [8] Xu, Z., Kibria, M. G., AlOtaibi, B., Duchesne, P. N., Besteiro, L. V., Gao, Y., Zhang, Q., Mi, Z., Zhang, P., Govorov, A. O., Mai, L., Chaker, M., and Ma, D. "Towards Enhancing Photocatalytic Hydrogen Generation: Which Is More Important, Alloy Synergistic Effect or Plasmonic Effect?" *Appl. Catal. B*, 221, 2018, pp. 77-85.
- [9] Bulliard, X., Jin, Y. H., Lee, G. H., Yun, S., Leem, D. -S., Ro, T., Park, K. - B., Heo, C. -J., Satoh, R. -I., Yagi, T., Choi, Y. S., Lim, S. -J., and Lee, S. "Dipolar Donor-Acceptor Molecules in the Cyanine Limit for High Efficiency Green-Light-Selective Organic Photodiodes." *J. Mater. Chem. C*, 4, 2016, pp. 1117-1125.
- [10] Jansen-van Vuuren, R. D., Pivrikas, A., Pandey, A. K., and Burn, P. L. "Colour Selective Organic Photodetectors Utilizing Ketocyanine-Cored Dendrimers." *J. Mater. Chem. C*, 1, 2013, pp. 3532-3543.
- [11] Lamprecht, B., Thünauer, R., Köstler, S., Jakopic, G., Leising, G., and Krenn, J. R. "Spectrally Selective Organic Photodiodes." *Phys. Status Solidi RRL*, 2, 2008, pp. 178-180.
- [12] Li, W., Li, S., Duan, L., Chen, H., Wang, L., Dong, G., and Xu, Z. "Squarylium and Rubrene based Filterless Narrowband Photodetectors for an All-Organic Two-Channel Visible Light Communication System." *Org. Electron.*, 37, 2016, pp. 346-351.
- [13] Sung, M. J., Yoon, S., Kwon, S. -K., Kim, Y. -H., and Chung, D. S. "Synthesis of

Phenanthro[1,10,9,8-*cdefg*]carbazole-Based Conjugated Polymers for Green-Selective Organic Photodiodes.” *ACS Appl. Mater. Interfaces*, 8, 2016, pp. 31172-31178.

[14] Deng, W., Huang, L., Xu, X., Zhang, X., Jin, X., Lee, S. -T., and Jie, J. “Ultrahigh-Responsivity Photodetectors from Perovskite Nanowire Arrays for Sequentially Tunable Spectral Measurement.” *Nano Lett.*, 17, 2017, pp. 2482-2489.

[15] Kim, K. -H., Ma, J. -Y., Moon, C. -K., Lee, J. -H., Baek, J. Y., Kim, Y. -H., and Kim, J. -J. “Controlling Emitting Dipole Orientation with Methyl Substituents on Main Ligand of Iridium Complexes for Highly Efficient Phosphorescent Organic Light-Emitting Diodes.” *Adv. Opt. Mater.*, 3, 2015, pp. 1191-1196.

[16] He, Z., Xiao, B., Liu, F., Wu, H., Yang, Y., Xiao, S., Wang, C., Russell, T. P., and Cao, Y. “Single-Junction Polymer Solar Cells with High Efficiency and Photovoltage.” *Nat. Photon.*, 9, 2015, pp. 174-179.

[17] Kim, I. K., Pal, B. N., Ullah, M., Burn, P. L., Lo, S. -C., Meredith, P., and Nanddas, E. B. “High-Performance, Solution-Processed Non-Polymeric Organic Photodiodes.” *Adv. Opt. Mater.*, 3, 2015, pp. 50-56.

[18] Jo, J. W., Jung, J. W., Bae, S., Ko, M. J., Kim, H., Jo, W. H., Jen, A. K. -Y., and Son, H. J. “Development of Self-Doped Conjugated Polyelectrolytes with Controlled Work Functions and Application to Hole Transport Layer Materials for High-Performance Organic Solar Cells.” *Adv. Mater. Interfaces*, 3, 2016, pp. 1500703.

[19] Huo, L., Liu, T., Cai, Y., Heeger, A. J., and Sun, Y. “Single-Junction Organic Solar Cells

Based on a Novel Wide-Bandgap Polymer with Efficiency of 9.7%.” *Adv. Mater.* 27, 2015, pp. 2938-2944.

[20] Kim, I. K., Li, X., Ullah, M., Shaw, P. E., Wawrzinek, R., Namdas, E. B., and Lo, S. -C. “High-Performance, Fullerene-Free Organic Photodiodes Based on a Solution-Processable Indigo.” *Adv. Mater.* 27, 2015, pp. 6390-6395.

[21] Yoon, S., Ha, J., Sim, K. M., Cho, W., and Chung, D. S. “Systematic Optimization of Low Bandgap Polymer/[6,6]-Phenyl C₇₀ Butyric Acid Methyl Ester Blend Photodiode via Structural Engineering.” *Org. Electron.* 35, 2016, pp. 17-23.

[22] Griffith, M. J., Willis, M. S., Kumar, P., Holdsworth, J. L., Bezuidenhout, H., Zhou, X., Belcher, W., and Dastoor, P. C. “Activation of Organic Photovoltaic Light Detectors Using Bend Leakage from Optical Fibers.” *ACS Appl. Mater. Interfaces*, 8, 2016, pp. 7928-7937.

[23] Osedach, T. P., Iacchetti, A., Lunt, R. R., Andrew, T. L., Brown, P. R., Akselrod, G. M., and Bulović, V. “Near-Infrared Photodetector Consisting of J-Aggregating Cyanine Dye and Metal Oxide Thin Films.” *Appl. Phys. Lett.*, 101, 2012, pp. 113303.

[24] Pierre, A., Deckman, I., Lechêne, P. B., and Arias, A. C. “High Detectivity All-Printed Organic Photodiodes.” *Adv. Mater.* 27, 2015, pp. 6411-6417.

[25] Chen, L., Xie, C., and Chen, Y. “Optimization of the Power Conversion Efficiency of Room Temperature-Fabricated Polymer Solar Cells Utilizing Solution Processed Tungsten Oxide and Conjugated Polyelectrolyte as Electrode Interlayer.” *Adv. Funct. Mater.*, 24, 2014, pp. 3986-3995.

- [26] Bogue, R. "Innovations in Image Sensing: A Review of Recent Research." *Sens. Rev.*, 34, 2014, pp. 143-148.
- [27] Sze, S. M. *Semiconductor Devices: Physics and Technology*, John Wiley & Sons, 2002, p.232.
- [28] Carrano, J. C., Li, T., Grudowski, P. A., Eiting, C. J., Dupuis, R. D., and Campbell, J. C. "High Quantum Efficiency Metal-Semiconductor-Metal Ultraviolet Photodetectors Fabricated on Single-Crystal GaN Epitaxial Layers." *Electron. Lett.*, 33, 1997, pp. 1980-1981.
- [29] Sfina, N., Yahyaoui, N., Said, M., and Lazzari, J. -L. "Modelling of the Quantum Transport in Strained Si/SiGe/Si Superlattices Based *p-i-n* Infrared Photodetectors for 1.3 - 1.55 μm Optical Communication." *Model. Numer. Simul. Mater. Sci.*, 4, 2014, pp. 37-52.
- [30] Lv, W., Peng, Y., Zhong, J., Luo, X., Li, Y., Zheng, T., Tang, Y., Du, L., and Peng, L. "Near Infrared Sensitive Organic Photodiode Utilizing Exciplex Absorption in $\text{NdPc}_2/\text{C}_{60}$ Heterojunction." *IEEE Photonics Tech. Lett.*, 27, 2015, pp. 2043-2046.
- [31] Armin, A., Jansen-van-Vuuren, R. D., Kopidakis, N., Burn, P. L., and Meredith, P. "Narrowband Light Detection via Internal Quantum Efficiency Manipulation of Organic Photodiodes." *Nat. Commun.*, 6, 2015, pp.6343.
- [32] Qi, B., and Wang, J. "Fill Factor in Organic Solar Cells." *Phys. Chem. Chem. Phys.*, 15, 2013, pp. 8972-8982.
- [33] Cowan, S. R., Leong, W. L., Banerji, N., Dennler, G., and Heeger, A. J. "Identifying a Threshold Impurity Level for Organic Solar Cells: Enhanced First-Order Recombination Via

Well-Defined PC₈₄BM Traps in Organic Bulk Heterojunction Solar Cells.” *Adv. Funct. Mater.*, 21, 2011, pp. 3083-3092.

[34] Giebink, N. C., Wiederrecht, G. P., Wasielewski, M. R., and Forrest, S. R. “Ideal Diode Equation for Organic Heterojunctions. I. Derivation and Application.” *Phys. Rev. B: Condens. Matter Mater. Phys.*, 82, 2010, pp. 155305.

[35] Guo, F., Xiao, Z., and Huang, J. “Fullerene Photodetectors with a Linear Dynamic Range of 90 dB Enabled by a Cross-Linkable Buffer Layer.” *Adv. Opt. Mater.*, 1, 2013, pp.289-294.

[36] Armin, A., Hambsch, M., Kim, I. K., Burn, P. L., Meredith, P., and Nardas, E. B. “Thick Junction Broadband Organic Photodiodes.” *Laser Photon. Rev.*, 8, 2014, pp. 924-932.

[37] Jang, M., Kim, S. H., Lee, H. -G., Kim, Y. -H., and Yang, H. “Layer-by-Layer Conjugated Extension of a Semiconducting Polymer for High-Performance Organic Field-Effect Transistor.” *Adv. Funct. Mater.*, 25, 2015, pp. 3833-3839.

[38] Sun, X., Lindner, J. -P., Bruchmann, B., and Schluter, A. D. “Synthesis of Neutral, Water-Soluble Oligo–Ethylene Glycol-Containing Dendronized Homo- and Copolymers of Generations 1, 1.5, 2, and 3.” *Macromolecules*, 47, 2014, pp. 7337-7346.

[39] Beiley, Z. M., Hoke, E. T., Noriega, R., Dacuna, J., Burkhard, G. F., Bartelt, J. A., Salleo, A., Toney, M. F., and McGehee, M. D. “Morphology-Dependent Trap Formation in High Performance Polymer Bulk Heterojunction Solar Cells.” *Adv. Energy Mater.*, 1, 2011, pp. 954–962.

[40] Yiu, A. T., Beaujuge, P. M., Lee, O. P., Woo, C. H., Toney, M. F., and Frechet, J. M. J. “Side-Chain Tunability of Furan-Containing Low Band-Gap Polymers Provides Control of

Structural Order in Efficient Solar Cells.” *J. Am. Chem. Soc.*, 134, 2012, pp. 2180-2185.

[41] Osaka, I., Saito, M., Mori, H., Koganezawa, T., and Takimiya, K. “Drastic Change of Molecular Orientation in a Thiazolothiazole Copolymer by Molecular-Weight Control and Blending with PC₆₁BM Leads to High Efficiencies in Solar Cells.” *Adv. Mater.*, 24, 2012, pp. 425-430.

[42] Stuart, A. C., Tumbleston, J. R., Zhou, H., Li, W., Liu, S., Ade, H., and You, W. “Fluorine Substituents Reduce Charge Recombination and Drive Structure and Morphology Development in Polymer Solar Cells.” *J. Am. Chem. Soc.*, 135, 2013, pp.1806-1815.

[43] Yip, H. L., and Jen, K.-Y. “Recent Advances in Solution-processed Interfacial Materials for Efficient and Stable Polymer Solar Cells.” *Energy Environ. Sci.*, 5, 2012, pp. 5994-6011.

[44] Shao, S., Zheng, K., Pullerits, T., and Zhang, F. “Enhanced Performance of Inverted Polymer Solar Cells by Using Poly(ethylene oxide)-Modified ZnO as an Electron Transport Layer.” *ACS Appl. Mater. Interfaces*, 5, 2013, pp. 380-385.

[45] Shimomura, M., Kawaguchi, T. K., Fukuda, Y., and Murakami, K. “Bidentate Chemisorption of Acetic Acid on a Si(001) – (2 × 1) Surface: Experimental and Theoretical Investigations.” *Phys. Rev. B: Condens. Matter Mater. Phys.*, 80, 2009, pp. 165324.

[46] Guo, F., Yang, B., Yuan, Y., Xiao, Z., Dong, Q., Bi, Y., and Huang, J. “A Nanocomposite Ultraviolet Photodetector Based on Interfacial Trap-Controlled Charge Injection.” *Nat. Nanotechnol.*, 7, 2012, pp. 798-802.

[47] Kim, H., Song, B., Lee, K., Forrest, S., and Kanicki, J. “Bilayer Interdiffused Heterojunction Organic Photodiodes Fabricated by Double Transfer Stamping.” *Adv. Opt. Mater.*, 5, 2017, pp.

1600784.

[48] Zhang, B., Trinh, M. T., Fowler, B., Ball, M., Xu, Q., Ng, F., Steigerwald, M. L., Zhu, X. -Y., Nuckolls, C., and Zhong, Y. "Rigid, Conjugated Macrocycles for High Performance Organic Photodetectors." *J. Am. Chem. Soc.*, 138, 2016, pp. 16426-16431.

[49] Lyons, D. M., Armin, A., Stolterfoht, M., Nagiri, R. C. R., Jansen-van Vuuren, R. D., Pal, B. N., Burn, P. L., Lo, S.-C., and Meredith, P. "Narrow Band Green Organic Photodiodes for Imaging." *Org. Electron.*, 15, 2014, pp. 2903-2911.

[50] Dong, R., Bi, C., Dong, Q., Guo, F., Yuan, Y., Fang, Y., Xiao, Z., and Huang, J. "An Ultra-violet-to-NIR Broad Spectral Nanocomposite Photodetector with Gain." *Adv. Opt. Mater.*, 2, 2014, pp. 549-554.

[51] Stolterfoht, M., Armin, A., Philippa, B., White, R. D., Burn, P. L., Meredith, P., Juska, G., and Pivrikas, A. "Photocarrier Drift Distance in Organic Solar Cells and Photodetectors." *Sci. Rep.*, 5, 2015, pp. 9949.

[52] Zhu, H. L., Cheng, J., Zhang, D., Liang, C., Reckmeier, C. J., Huang, H., Rogach, A. L., and Choy, W. C. H. "Room-Temperature Solution-Processed NiO_x: PbI₂ Nanocomposite Structures for Realizing High-Performance Perovskite Photodetectors." *ACS Nano*, 10, 2016, pp. 6808-6815.

[53] Horie, Y., Han, S., Lee, J. -Y., Kim, J., Kim, Y., Arbabi, A., Shin, C., Shi, L., Arbabi, E., Kamali, S. M., Lee, H. -S., Hwang, S., and Faraon, A. "Visible Wavelength Color Filters Using Dielectric Subwavelength Gratings for Backside-Illuminated CMOS Image Sensor

Technologies.” *Nano Lett.*, 17, 2017, pp. 3159-3164.

[54] Yamamoto, K., Nakajima, A., Yoshimi, M., Sawada, T., Fukuda, S., Suezaki, T., Ichikawa, M., Koi, Y., Goto, M., Meguro, T., Matsuda, T., Kondo, M., Sasaki, T., and Tawada, Y. “A High Efficiency Thin Film Silicon Solar Cell and Module.” *Sol. Energy*, 77, 2004, pp. 939-949.

[55] Wu, X. D., Inam, A., Hegde, M. S., Wilkens, B., Chang, C. C., Hwang, D. M., Nazar, L., Venkatesan, T., Miura, S., Matsubara, S., Miyasaka, Y., and Shohata, N. “High Critical Currents in Epitaxial $\text{YBa}_2\text{Cu}_3\text{O}_{7-x}$ Thin Films on Silicon with Buffer Layers.” *Appl. Phys. Lett.*, 54, 1989, pp. 754-756.

[56] Vezie, M. S., Few, S., Meager, I., Pieridou, G., Dörling, B., Ashraf, R. S., Goñi, A. R., Bronstein, H., McCulloch, I., Hayes, S. C., Campoy-Quiles, M., and Nelson, J. “Exploring the Origin of High Optical Absorption in Conjugated Polymers.” *Nat. Mater.*, 15, 2016, pp. 746-753.

[57] Konstantatos, G., and Sargent, E. H. “Nanostructured Materials for Photon Detection.” *Nat. Nanotech.*, 5, 2010, pp. 391-400.

[58] Yoon, S., Ha, J., Cho, J., and Chung, D. S. “Nonabsorbing Acceptor-Based Planar Heterojunction for Color-Selective and High-Detectivity Polymer Photodiodes.” *Adv. Opt. Mater.*, 4, 2016, pp. 1933-1938.

[59] Han, M. G., Park, K. -B., Bulliard, X., Lee, G. H., Yun, S., Leem, D. -S., Heo, C. -J., Yagi, T., Sakurai, R., Ro, T., Lim, S. -J., Sul, S., Na, K., Ahn, J., Jin, Y. W., and Lee, S. “Narrow-Band Organic Photodiodes for High-Resolution Imaging.” *ACS Appl. Mater. Interfaces*, 8, 2016, pp. 26143-26151.

- [60] Ko, S. -J., Walker, B., Nguyen, T. L., Choi, H., Seifter, J., Uddin, M. A., Kim, T., Kim, S., Heo, J., Kim, G. -H., Cho, S., Heeger, A. J., Woo, H. Y., and Kim, J. Y. "Photocurrent Extraction Efficiency near Unity in a Thick Polymer Bulk Heterojunction." *Adv. Funct. Mater.*, 26, 2016, pp. 3324-3330.
- [61] Uddin, M. A., Lee, T. H., Xu, S., Park, S. Y., Kim, T., Song, S., Nguyen, T. L., Ko, S. -J., Hwang, S., Kim, J. Y., and Woo, H. Y. "Interplay of Intramolecular Noncovalent Coulomb Interactions for Semicrystalline Photovoltaic Polymers." *Chem. Mater.*, 27, 2015, pp. 5997-6007.
- [62] Nguyen, T. L., Choi, H., Ko, S. -J., Uddin, M. A., Walker, B., Yum, S., Jeong, J. -E., Yun, M. H., Shin, T. J., Hwang, S., Kim, J. Y., and Woo, H. Y. "Semi-Crystalline Photovoltaic Polymers with Efficiency Exceeding 9% in a ~300 nm Thick Conventional Single-Cell Device." *Energy Environ. Sci.*, 7, 2014, pp. 3040-3051.
- [63] Chung, D. S., Park, J. W., Kim, S. -O., Heo, K., Park, C. E., Ree, M., Kim, Y. -H., and Kwon, S. -K. "Alternating Copolymers Containing Bithiophene and Dialkoxynaphthalene for the Application to Field Effect Transistor and Photovoltaic Cell: Performance and Stability." *Chem. Mater.*, 21, 2009, pp. 5499-5507.
- [64] Kim, K., Sim, K. M., Yoon, S., Jang, M. S., and Chung, D. S. "Defect Restoration of Low-Temperature Sol-Gel-Derived ZnO via Sulfur Doping for Advancing Polymeric Schottky Photodiodes." *Adv. Funct. Mater.*, 28, 2018, pp.1802582.
- [65] Pettersson, L. A. A., Roman, L. S., and Inganäs, O. "Modeling Photocurrent Action Spectra of Photovoltaic Devices Based on Organic Thin Films." *J. Appl. Phys.*, 86, 1999, pp. 487-496.

- [66] Burkhard, G. F., Hoke, E. T., and McGehee, M. D. "Accounting for Interference, Scattering, and Electrode Absorption to Make Accurate Internal Quantum Efficiency Measurements in Organic and Other Thin Solar Cells." *Adv. Mater.*, 22, 2010, pp. 3293-3297.
- [67] Pina, J., de Melo, J. S., Burrows, H. D., Galbrecht, F., Nehls, B. S., Farrell, T., and Scherf, U. "Spectral and Photophysical Studies of Poly[2,6-(1,5-dioctylnaphthalene)]thiophenes." *J. Phys. Chem. C*, 111, 2007, pp. 7185-7191.
- [68] Sun, Y., Seo, J. H., Takacs, C. J., Seifert, J., and Heeger, A. J. "Inverted Polymer Solar Cells Integrated with a Low-Temperature-Annealed Sol-Gel-Derived ZnO Film as an Electron Transport Layer." *Adv. Mater.*, 23, 2011, pp. 1679-1683.
- [69] Kaya, E., Turan, N., Gündüz, B., Çolak, N., and Körkoca, H. "Synthesis, Characterization of Poly-2-(2-hydroxybenzylideneamino)-6-phenyl-4,5,6,7-tetrahydrobenzo[*b*]thiophene-3-carbonitrile: Investigation of Antibacterial Activity and Optical Properties." *Polym. Eng. Sci.*, 52, 2012, pp. 1581-1589.
- [70] Mihailetschi, V. D., van Duren, J. K. J., Blom, P. W. M., Hummelen, J. C., Janssen, R. A. J., Kroon, J. M., Rispen, M. T., Verhees, W. J. H., and Wienk, M. M. "Electron Transport in a Methanofullerene." *Adv. Funct. Mater.*, 13, 2003, pp. 43-46.
- [71] Mori, T., and Kijima, M. "Synthesis and Optical Properties of Polynaphthalene Derivatives." *Opt. Mater.*, 30, 2007, pp. 545-552.
- [72] Street, R. A., Mulato, M., Lau, R., Ho, J., Graham, J., Popovic, Z., and Hor, J. "Image Capture Array with an Organic Light Sensor." *Appl. Phys. Lett.*, 78, 2001, pp. 4193-4195.

- [73] Collins, B. A., Tumbleston, J. R., and Ade, H. “Miscibility, Crystallinity and Phase Development in P3HT/PCBM Solar Cells: Toward an Enlightened Understanding of Device Morphology and Stability.” *J. Phys. Chem. Lett.*, 2, 2011, pp. 3135-3145.
- [74] Gupta, V., Kyaw, A. K. K., Wang, D. H., Chand, S., Bazan, G. C., and Heeger, A. J. “Barium: An Efficient Cathode Layer for Bulk heterojunction Solar Cells.” *Sci. Rep.*, 3, 2013, pp. 1965.
- [75] Kielar, M., Dhez, O., Pecastaings, G., Curutchet, A., and Hirsch, L. “Long-Term Stable Organic Photodetectors with Ultra Low Dark Currents for High Detectivity Applications.” *Sci. Rep.*, 6, 2016, pp.39201.
- [76] Konstantatos, G., Clifford, J., Levina, L., and Sargent, E. H. “Sensitive Solution-Processed Visible-Wavelength Photodetectors.” *Nat. Photon.*, 1, 2007, pp. 531-534.
- [77] Asif Khan, M., Kuznia, J. N., Olson, D. T., Van Hove, J. M., Blasingame, M., and Reitz, L. F. “High-Responsivity Photoconductive Ultraviolet Sensors Based on Insulating Single-Crystal GaN Epilayers.” *Appl. Phys. Lett.*, 60, 1992, pp. 2917-2919.
- [78] Fang, Y., Dong, Q., Shao, Y., Yuan, Y., and Huang, J. “Highly Narrowband Perovskite Single-Crystal Photodetectors Enabled by Surface-Charge Recombination.” *Nat. Photon.*, 9, 2015, pp. 679-686.
- [79] Hassan, S. Z., Cheon, H. J., Choi, C., Yoon, S., Kang, M., Cho, J., Jang, Y. H., Kwon, S. - K., Chung, D. S., and Kim, Y. -H. “Molecular Engineering of a Donor–Acceptor Polymer to Realize Single Band Absorption toward a Red-Selective Thin-Film Organic Photodiode.” *ACS*

Appl. Mater. Interfaces, 11, 2019, pp. 28106-28114.

[80] Lin, Q., Armin, A., Burn, P. L., and Meredith, P. “Filterless Narrowband Visible Photodetectors.” *Nat. Photon.*, 9, 2015, pp. 687-694.

[81] Sim, K. M., Yoon, S., Cho, J., Jang, M. S., and Chung, D. S. “Facile Tuning the Detection Spectrum of Organic Thin Film Photodiode via Selective Exciton Activation.” *ACS Appl. Mater. Interfaces*, 10, 2018, pp. 8405-8410.

[82] Esopi, M. R., Zheng, E., Zhang, X., Cai, C., and Yu, Q. “Tuning the Spectral Response of Ultraviolet Organic–Inorganic Hybrid Photodetectors via Charge Trapping and Charge Collection Narrowing.” *Phys. Chem. Chem. Phys.*, 20, 2018, pp. 11273-11284.

[83] Kim, S. -K., Park, S., Son, H. J., and Chung, D. S. “Synthetic Approach to Achieve a Thin-Film Red-Selective Polymer Photodiode: Difluorobenzothiadiazole-Based Donor–Acceptor Polymer with Enhanced Space Charge Carriers.” *Macromolecules*, 51, 2018, pp. 8241-8247

[84] Wang, W., Zhang, F., Du, M., Li, L., Zhang, M., Wang, K., Wang, Y., Hu, B., Fang, Y., and Huang, J. “Highly Narrowband Photomultiplication Type Organic Photodetectors.” *Nano Lett.*, 17, 2017, pp. 1995-2002.

[85] Miao, J., Zhang, F., Du, M., Wang, W., and Fang, Y. “Photomultiplication Type Organic Photodetectors with Broadband and Narrowband Response Ability.” *Adv. Opt. Mater.*, 6, 2018, pp. 1800001.

[86] Saidaminov, M. I., Haque, Md. A., Savoie, M., Abdelhady, A. L., Cho, N., Dursun, I., Buttner, U., Alarousu, E., Wu, T., and Bakr, O. M. “Perovskite Photodetectors Operating in Both

Narrowband and Broadband Regimes.” *Adv. Mater.*, 28, 2016, pp. 8144-8149.

[87] Liu, R., Lee, S. -T., and Sun, B. “13.8% Efficiency Hybrid Si/Organic Heterojunction Solar Cells with MoO₃ Film as Antireflection and Inversion Induced Layer.” *Adv. Mater.*, 26, 2014, pp. 6007-6012.

[88] Jiang, Y., Xiao, S., Xu, B., Zhan, C., Mai, L., Lu, X., and You, W. “Enhancement of Photovoltaic Performance by Utilizing Readily Accessible Hole Transporting Layer of Vanadium(V) Oxide Hydrate in a Polymer–Fullerene Blend Solar Cell.” *ACS Appl. Mater. Interfaces*, 8, 2016, pp. 11658-11666.

[89] Abu-Safia, H., Al-Tahtamouni, R., Abu-Aljarayesh, I., and Yusuf, N. A. “Transmission of a Gaussian Beam through a Fabry–Perot Interferometer.” *Appl. Opt.*, 33, 1994, pp. 3805-3811

[90] Jansen van Vuuren, R., Johnstone, K. D., Ratnasingam, S., Barcena, H., Deakin, P. C., Pandey, A. K., Burn, P. L., Collins, S., and Samuel, I. D. W. “Determining the Absorption Tolerance of Single Chromophore Photodiodes for Machine Vision.” *Appl. Phys. Lett.*, 96, 2010, pp. 253303.

[91] Lapray, P. -J., Thomas, J. -B., Gouton, P., and Ruichek, Y. “Energy Balance in Spectral Filter Array Camera Design.” *J. Eur. Opt. Soc. –Rapid Publ.*, 13, 2017, pp. 1.

[92] Mohamed, S. A., Gasiorowski, J., Hingerl, K., Zahn, D. R. T., Scharber, M. C., Obayya, S. S. A., El-Mansy, M. K., Sariciftci, N. S., Egbe, D. A. M., and Stadler, P. “CuI as Versatile Hole-Selective Contact for Organic Solar Cell based on Anthracene-Containing PPE–PPV.” *Sol. Energy Mater. Sol. Cells*, 143, 2015, pp. 369-374.

- [93] Shrotriya, V., Li, G., Yao, Y., Chu, C. – W., and Yang, Y. “Transition Metal Oxides as the Buffer Layer for Polymer Photovoltaic Cells.” *Appl. Phys. Lett.*, 88, 2006, pp. 073508.
- [94] Dou, L., Yang, Y. M., You, J., Hong, Z., Chang, W. -H., Li, G., and Yang, Y. “Solution-Processed Hybrid Perovskite Photodetectors with High Detectivity.” *Nat. Commun.*, 5, 2014, pp. 5404.
- [95] Lin, Q., Armin, A., Lyons, D. M., Burn, P. L., and Meredith, P. “Low Noise, IR-Blind Organohalide Perovskite Photodiodes for Visible Light Detection and Imaging.” *Adv. Mater.*, 27, 2015, pp. 2060-2064.
- [96] Xiong, S., Li, L., Qin, F., Mao, L., Luo, B., Jiang, Y., Li, Z., Huang, J., and Zhou, Y. “Universal Strategy to Reduce Noise Current for Sensitive Organic Photodetectors.” *ACS Appl. Mater. Interfaces*, 9, 2017, pp. 9176-9183.
- [97] Nie, R., Deng, X., Feng, L., Hu, G., Wang, Y., Yu, G., and Xu, J. “Highly Sensitive and Broadband Organic Photodetectors with Fast Speed Gain and Large Linear Dynamic Range at Low Forward Bias.” *Small*, 13, 2017, pp. 1603260.
- [98] Lee, K. - H., Leem, D. - S., Castrucci, J. S., Park, K. - B., Bulliard, X., Kim, K. - S., Jin, Y. W., Lee, S., Bender, T. P., and Park, S. Y. “Green-Sensitive Organic Photodetectors with High Sensitivity and Spectral Selectivity Using Subphthalocyanine Derivatives.” *ACS Appl. Mater. Interfaces*, 5, 2013, pp. 13089-13095.
- [99] Pandey, A. K., Johnstone, K. D., Burn, P. L., and Samuel, I. D. W. “Solution-Processed Pentathiophene Dendrimer based Photodetectors for Digital Cameras.” *Sens. Actuators, B*, 196,

2014, pp. 245-251.

[100] Lee, W., Lee, J., Yun, H., Kim, J., Park, J., Choi, C., Kim, D. C., Seo, H., Lee, H., Yu, J. W., Lee, W. B., and Kim, D. -H. "High-Resolution Spin-on-Patterning of Perovskite Thin Films for a Multiplexed Image Sensor Array." *Adv. Mater.*, 29, 2017, pp. 1702902.

[101] Takeda, Y., Hayasaka, K., Shiwaku, R., Yokosawa, K., Shiba, T., Mamada, M., Kumaki, D., Fukuda, K., and Tokito, S. "Fabrication of Ultra-Thin Printed Organic TFT CMOS Logic Circuits Optimized for Low-Voltage Wearable Sensor Applications." *Sci. Rep.*, 6, 2016, pp. 25714.

5 국문 요약

컬러 필터 배제형 이미지 센서를 위한 유기 광다이오드의 접합 공학

2018년 2월, Panasonic사에서 최초로 광활성층으로 실리콘 기반 무기 반도체 대신 유기 반도체를 적용한 CMOS 이미지 센서를 공개하였다. 이처럼, 유기 이미지 센서는 실험적 단계를 넘어, 점차 상용화 단계로 접어들고 있다. 하지만 공개된 유기 CMOS 이미지 센서를 포함하여, 기존의 이미지 센서는 모두 파장 선택성이 없는 전색성 흡광을 보이는 광활성 소재를 사용하여, 입사광의 색의 구분을 위해 컬러 필터의 사용이 강제되고 있다. 이러한 컬러 필터는 컬러 필터 자체의 두께에 따른 집적도의 제한뿐만 아니라, 컬러 필터 제작을 위한 추가적인 공정 시간 및 비용과 같은 많은 단점을 동반한다고 할 수 있다. 따라서, 이를 극복하기 위해, 현재 이미지 센서 구조에서 컬러 필터를 제거하는 것이 화두로 떠오르고 있다.

본 논문은 기존 이미지 센서의 개선을 위해, 이미지 센서의 단위 소자인 포토다이오드에 대한 연구로, 최종적으로는 컬러 필터 없이 파장 선택성 및 고성능을 구현할 수 있도록 하기 위한 세 가지 접근법에 대해 다룬다. 첫 번째로, 고분자 전해질(Polyelectrolyte)을 전극과 광활성층 사이의 중간층(Interlayer)으로 적용하여, 고성능 유기 포토다이오드를 구현하였다. 고분자 전해질을 ITO/ZnO 투명 전극과 광활성층 사이에 적용하여, 투명 전극의 일함수를 소자의 암전류 억제 및 광전류 향상에 유리한 방향으로 자유로이 조절할 수 있을 뿐만 아니라, ZnO에 존재하는 표면 트랩(Surface trap)을 제거하여, 결과적으로 광전류의 향상과 암전류의 억제를 동시에 달성하여, 감광 성능의 유의미한 향상을 보였다.

두 번째 접근법으로, 파장 선택성을 보이는 전자 주개(Donor) 반도체 소재와 투명 전극의 쇼트키 접합(Schottky junction)을 적용하여, 파장 선택성 반도체 소재의 흡광 스펙트럼이 온전히 감광 스펙트럼으로 반영되도록 하였다. 상기 방법을 이용하여 형성한 파장 선택성 유기 포토다이오드의 추가적인 성능 향상을 위해, 소량의 전자 받개(Acceptor) 반도체 소재를 전자 주개 소재에 첨가하였고, 이를 통해 쇼트키 접합 특성을 해치지 않으면서도 전자 주개-전자 받개 계면을 새로이 형성하여, 암전류의 향상을 최대한 억제하는 선에서 광전류의 향상을 끌어낼 수 있었다. 또한, 투명 전극을 구성하는 소재인 ZnO와 파장 선택성 유기 반도체 소재의 정밀한 두께 조절을 통해, 원하는 파장 영역에 대한 흡광은 동일한 수준을 유지하면서도 원치 않는 파장 영역에 대한 흡광을 최소화하여, 파장 선택성을 극대화할 수 있었다.

마지막 접근법으로, 기존 이미지 센서 내 투명 전극 위치에 파장 선택성을 지니는 에탈론 전극을 적용하여, 컬러 필터를 사용한 포토다이오드에 비견할 만한 파장 선택성을 컬러 필터 없이 구현할 수 있었다. 또한, 에탈론 전극은 열증착법을 이용해 제작하게 되는데, 따라서 용액 공정에 비해 보다 손쉬운 패턴이 가능하다고 할 수 있다. 이를 이용하여, 적/녹/청색광 선택성 유기 포토다이오드를 10×10 구조로 배치하여 형성한 간이 이미지 센서를 이용하여, 풀 컬러 이미지를 컬러 필터 없이 촬영할 수 있었다.

핵심어: 유기 광다이오드, 유기 이미지 센서, 접합 공학, 에탈론 전극, 고성능